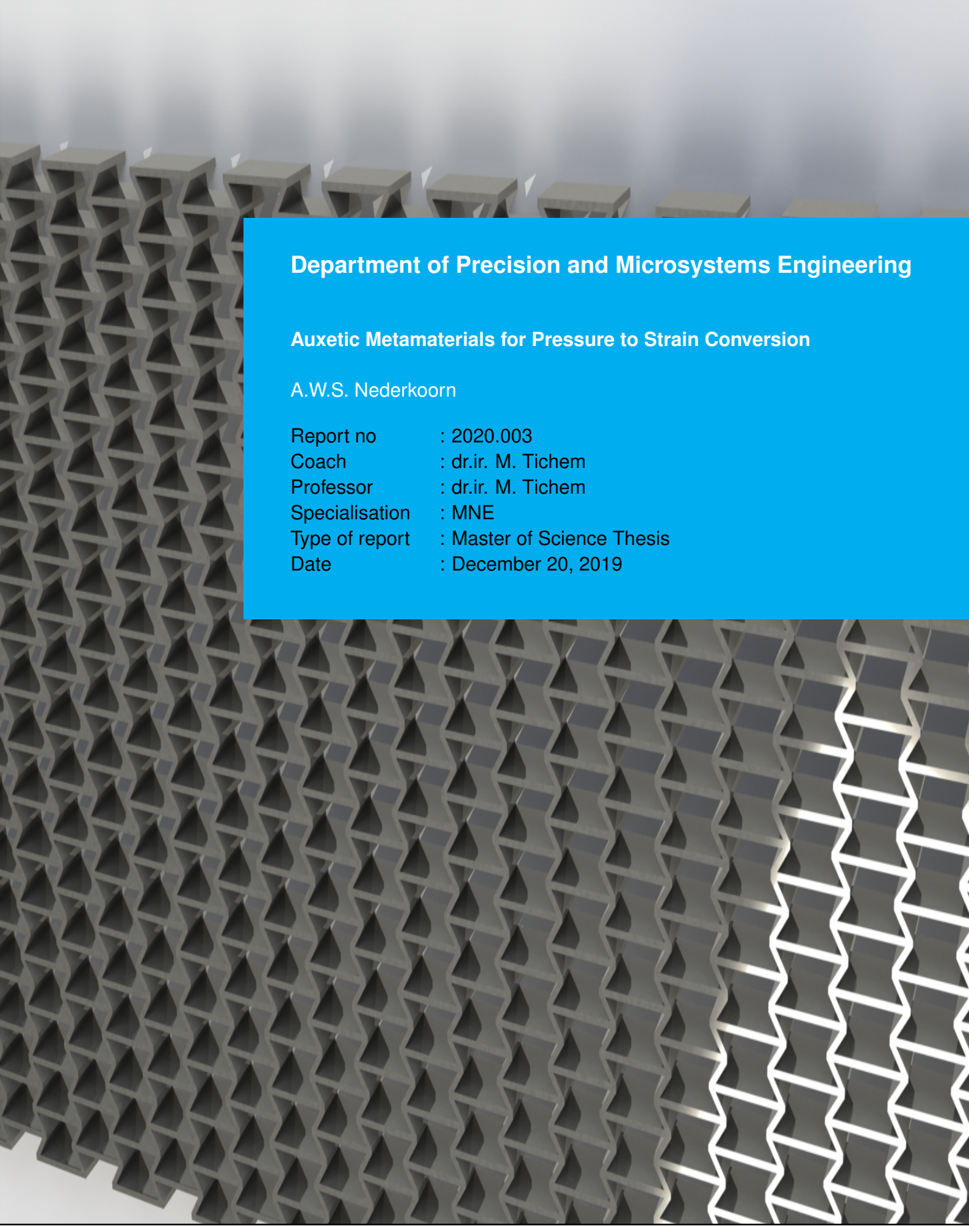

Department of Precision and Microsystems Engineering

Auxetic Metamaterials for Pressure to Strain Conversion

A.W.S. Nederkoorn

Report no : 2020.003
Coach : dr.ir. M. Tichem
Professor : dr.ir. M. Tichem
Specialisation : MNE
Type of report : Master of Science Thesis
Date : December 20, 2019

TU Delft Delft University of Technology

High Tech Engineering - 3Me

Auxetic Metamaterials for Pressure to Strain Conversion

Master of Science Thesis

For the degree of Master of Science in Mechanical Engineering at Delft University of Technology

A.W.S. Nederkoorn

December 20, 2019

This thesis is confidential and cannot be made public until December 20, 2021.

Faculty of Mechanical, Maritime and Materials Engineering (3mE) · Delft University of Technology

Abstract

The purpose of this study is to investigate how metamaterials with a negative Poisson ratio, so-called auxetic metamaterials, can be used for conversion of pressure from a fluid to strain in a solid for application in a medical pressure sensor.

As a first step, a literature review was carried out to identify the potential of auxetic metamaterials as a solution direction for pressure to strain conversion. From considering three optimal case scenarios for solution directions to create strain in a fiber, the approach of auxetic metamaterials stood out. High axial strains and a linear straining behavior, which is important for the read-out of the sensor, were expected.

Auxetic Chiral structures were designed and fabricated and their effective Poisson ratios were experimentally evaluated. It was found that the boundary effects that are introduced during experiments influence the behavior of the auxetic structure, especially on the unit cells close to the boundaries. A region was found where the unit-cells behave as theory describes and the boundary effects are dissipated. Additionally, it was found that for the an-isotropic Meta Tetra Chiral structure the Poisson ratio is influenced by applied strain. The isotropic Anti Tetra Chiral structure did not show strain dependent behavior.

The relation between pressure to strain conversion and the effective properties of auxetic structures indicated that an-isotropic effective properties are preferred. Using this finding Re-entrant Honeycomb structures were designed for high pressure to strain conversion. From measuring the force input and output while deforming the structure, the expectations were verified.

In this research it was found that auxetic metamaterials with an-isotropic effective properties, such as Re-entrant Honeycomb structures, are an effective intermediate for converting pressure from the fluid domain to strain in a fiber.

Table of Contents

Acknowledgements

I wish to show my gratitude to my supervisor dr. ir. Marcel Tichem. With his enthusiasm and expertise on the subject, he guided me through the process of completing this study. He taught me that by looking with a critical view at your own work and that of others, you push yourself to perform. I would like to thank the technical support staff for helping me realize my experiments. Patrick van Holst helped me in carrying out compression experiments. Additionally, his insights helped me defining and building my experimental setup. I wish to thank Bradley But who assisted me in the fabrication of the auxetic structures using additive manufacturing. I want to show my gratitude to Jos van Driel who helped me in realizing the sensory part of my experiments, including choosing the right sensors, calibration and designing the read-out software system. I would like to recognize the support of my friends from room F250-3ME, for keeping me company during the summer. Finally, I want to thank my parents for their unconditional support in realizing my dreams and engineering studies.

Delft, University of Technology A.W.S. Nederkoorn
December 20, 2019

Chapter 1

Introduction

Problem Statement

Cardiovascular diseases are estimated to cause 31% of deaths globally [1]. A common heart disease is Atherosclerosis, which means that the blood flow in the artery is disturbed by a narrowing or blockage [2]. Angioplasty is an intervention procedure for opening obstructed arteries through the placement of cylindrical structures also called stents [3]. Currently, surgeons use Röntgen imaging to locate the arterial blockages. In order to improve the speed and quality of the procedure and to minimize dependency on harmful Röntgen techniques, development of a novel methodology to detect the location of obstructions is necessary.

Strictures in an artery cause a local deviation in blood pressure. A method of measuring pressure is through the use of a Fiber Bragg Grating (FBG) Sensor [4]. This method has certain advantages in the field of medical application, over conventional methods. Firstly, the optical fiber is not affected by magnetic interference [4], making it possible to use in combination with an MRI scanner. Secondly, the typical fiber diameter used for Fiber Bragg Grating sensors is 125 μm [5], which makes it suitable to measure pressure inside arteries or veins.

Creating a periodic change of refractive index, a so called *Bragg* grating, inside the core of an optical fiber results in the reflection of a specific part of the spectrum passed through the fiber. The periodicity of the grating determines the reflected wavelength, also called the Bragg wavelength. The working principle of FBG sensors is based on the axial strain inside the optical fiber that changes the periodicity of the grating and results in a shift in the reflected Bragg wavelength [6]. For improvement of the pressure sensitivity of these devices the amount of axial strain that is caused by the to-be-measured pressure is of importance. One approach to improve pressure sensitivity is the use of Mechanical Metamaterials, which are hierarchically structured materials that can be designed for unconventional material properties. Auxetic Metamaterials is a class of materials that can achieve negative Poisson ratios [7], meaning the material shrinks in horizontal direction when compressed in vertical direction. This is beneficial as pressure from all sides of the material will lead to a strain in the same direction, and thus could improve pressure sensitivity in FBG sensors.

In this study the solution direction of auxetic metamaterials for converting pressure to strain in a Fiber Bragg Grating sensor is investigated.

Research Questions

To solve the problem that is described above and to investigate the potential of this new solution direction, the following research question is formulated.

How can auxetic metamaterials be used as an intermediate for converting pressure from the fluid domain to strain in the mechanical domain?

In order to answer this research question the following subquestions have to be answered:

1. How does the approach of auxetic metamaterials compare to currently known solutions for converting pressure to strain in a solid body?
2. How can the effective Poisson ratio, that the unit-cell is designed for be accurately verified, using experimental methods :
   (a) What is the effect of boundaries, fixed or free, on the behavior of the structure and what does this mean for the effective Poisson ratio?
   (b) How do individual unit-cells behave within a structure, considering these boundary effects?
   (c) Does the amount of strain affect the behavior of the structure and thus the effective Poisson ratio?
3. What are potentially well performing auxetic structural designs to convert pressure to strain in a body?
   (a) What is the connection between the effective material properties of an auxetic metamaterial and the ability to amplify strain?
   (b) Which auxetic metamaterial basic structure type is best suited and what are the expected limits for pressure to strain conversion?

This report describes the results of the research carried out to answer these questions. First, a literature review has been performed in order to investigate auxetic metamaterials, fiber Bragg grating sensors and existing solutions for amplifying pressure to strain. This full review is described in a separate report [8]. A concise summary of the reasoning and findings of this review is included in chapter 2, in order to illustrate the potential of auxetic metamaterials as a solution direction for pressure to strain amplification compared to existing solutions.

Next, in chapter 3, a methodology to experimentally verify the effective properties for which a structure is theoretically designed is described. In this part, the boundary effects introduced when experimentally measuring the effective Poisson ratio, the Poisson ratio per unit-cell and the effect of strain on the Poisson ratio are investigated.

Chapter 4 focuses on the application of auxetic metamaterials specifically to convert pressure from the fluid domain to strain in a solid. First, the relation between effective properties, such as the Poisson ratio and the Young Modulus, and strain transfer is considered to determine what structure type is suitable for this application. After having selected a structure

type based on this relation, the effect of the structure geometry on strain amplification is investigated and experimentally verified.

In chapter 5 the final conclusion with respect to the main research question of how an auxetic structure can be designed for pressure to strain amplification is presented. Additionally, recommendations for future research are discussed here.

Chapter 2

Auxetic Metamaterials: An Introduction

In this chapter a concise summary is given of the results from a literature review that has been performed in preparation of this current study. The full literature review is documented in another report titled: *Potential of Metamaterials for Improving Pressure Sensitivity of Fiber Bragg Grating Sensors* [8]. In the review [8] the state of the art of Fiber Bragg Grating sensors and mechanical metamaterials is discussed. The second part of the review [8] is an analysis of the performance of conventional solutions as well as of a new solution direction considering auxetic metamaterials.

First, the background of mechanical metamaterials is introduced, specifically the auxetic mechanical metamaterial. To answer the first research question and to provide the basis for the rest of this current study, the concept of using an auxetic metamaterial as a solution direction for this problem is explained.

Three optimal cases of different solution directions are analyzed. Concluding this chapter, an overview is given of the expected performance of conventional solution directions versus the solution using auxetic metamaterials.

2-1 Auxetic Metamaterials

Mechanical metamaterials are a class of materials with uncommon material properties, which are achieved by structures within the material itself. Examples of this can be found in nature, such as cork or bone tissue. In nature this phenomenon is produced through evolution. The recent developments in manufacturing techniques make it possible for researchers to use this concept from nature and build their own hierarchical structured metamaterials at the nanometer scale [9]. For the purpose of this study one particular type of metamaterials is interesting, the auxetic metamaterial. This type of mechanical metamaterials has a negative Poisson ratio. The Poisson ratio defines the amount of orthogonal strain that occurs due to

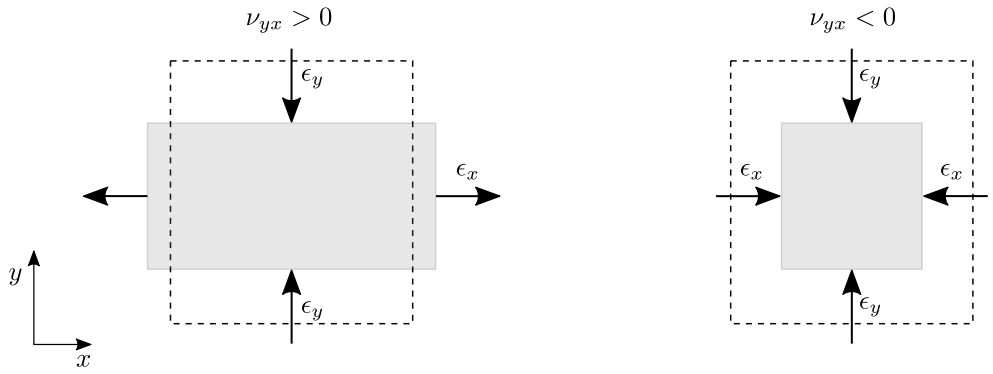

Figure 2-1: Schematic illustrating the Poisson ratio, v_{yx}.

the strain created in the loading direction, as seen in Equation 2-1. The effect for a regular and negative Poisson ratio is shown in Figure 2-1.

$$\nu_{yx} = -\frac{\epsilon_x}{\epsilon_y} \tag{2-1}$$

Auxetic metamaterials can be created with a number of approaches. In Figure 2-2 an overview the different types and classes of auxetic structures that are described in literature. The first distinction is made between a hierarchical auxetic metamaterial, which is a material structure, that is built out unit-cells that also have a particular structure [10] and unstructured materials like foams which can also show auxetic behavior [7]. For the most complete overview of all the different classes, types and developments of the past three decades in the field of auxetic metamaterials refer to [11]. Within the hierarchical auxetic structures, a new subdivision can be made between Chiral structures, Re-entrant structures and rotating shapes.

Chiral structures are built from unit-cells that consist of a rigid ring and a number of beams, or *ligaments*. The auxetic behavior is caused by the rotation of the rigid rings.

Re-entrant structures are designed to contract or bend inward, by positioning of the beams.

Rotating shapes is structure class with structures designed out of hinging planes with a specific shape.

Within these structure *classes*, there are numerous of different possible *types*, which can be designed for specific effective properties.

For the purpose of this study, the interesting structures types are hierarchical structures, as they can be designed for effective material properties using theory from literature. In Appendix A, the derivation of effective material properties of the archetypes of the Chiral and Re-entrant structure classes is found.

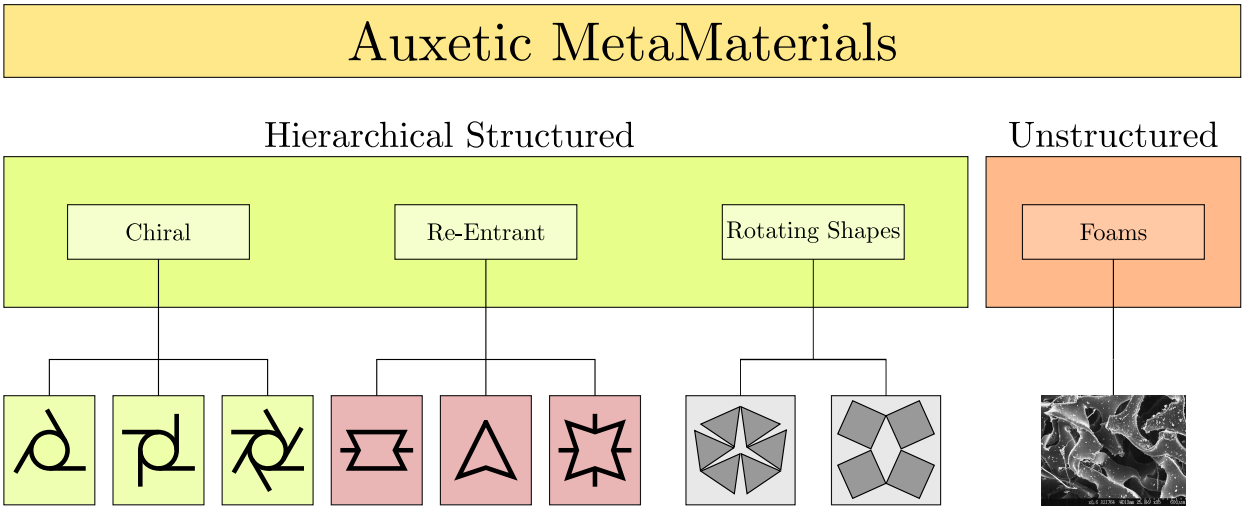

Figure 2-2: An Overview of Auxetic Structure Types

2-2 Optimal Cases

In this section, an optimal case for the two most interesting approaches following from the analysis in [8] and the solution direction using auxetic metamaterials, are considered. These optimal cases are analyzed both theoretically and with a FEM analysis. This is to get an idea of the maximum achievable gain in pressure to strain conversion, for each concept. First, the structural approach is considered. Next, the bending approach is discussed. Thereafter the Auxetic metamaterial is considered. Finally, a comparative overview is given.

Design Constraints

The design space and requirements for the sensor are given by the fact that the sensor has to be able to operate in an artery and measure blood pressure. The requirements are:

A maximum sensor node diameter of 330 μm

A minimum measurable pressure difference of 134 Pa
This corresponds to 1 millimeter of mercury (mm Hg), which is the standard unit for pressure used in medicine

In addition to the requirements the dimensions and properties of the optical fiber is given. The minimum achievable diameter of a glass fiber is considered as 50 μm. The Young Modulus of an optical fiber used for Fiber Bragg Gratings is $E_f = 72$ GPa [12]. The minimum measurable pressure difference of 134 Pa corresponds to 0.1 nanostrain Pa^{-1} in the Fiber Bragg Grating sensor.

2-2-1 Structural Approach

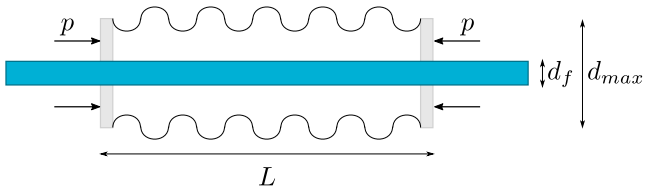

Figure 2-3: Schematic of the structural approach.

The structural approach is based on increasing the area on which the pressure acts while keeping the cross-sectional area of the strained body as small as possible. An optimal representation of this idea, is shown in Figure 2-3. The axial pressure acts on the rigid disks of diameter $d_{max} = 330$ μm, this causes axial strain in the fiber with diameter $d_f = 50$ μm. The contribution of the bellows on the straining behavior in the optical fiber is not considered in this calculation. Including the mechanics of the bellows leads to a contribution in axial stiffness of the total system. Additionally, bending of the bellows due to pressure leads to a compressive axial strain in the fiber.

The axial stress, caused by pressure p on the disk, in the fiber is obtained as,

$$\sigma_x = p\frac{A_D}{A_f} \tag{2-2}$$

With A_D as the area of the disk and A_f as the cross sectional area of the glass fiber. Using Hooke's law ($E_f = \sigma_x/\epsilon_x$), results in the axial strain. Following this method with $E_f = 72$ GPa, the achievable axial strain in the fiber is $\epsilon_x = 0.59$ nanostrain Pa^{-1}

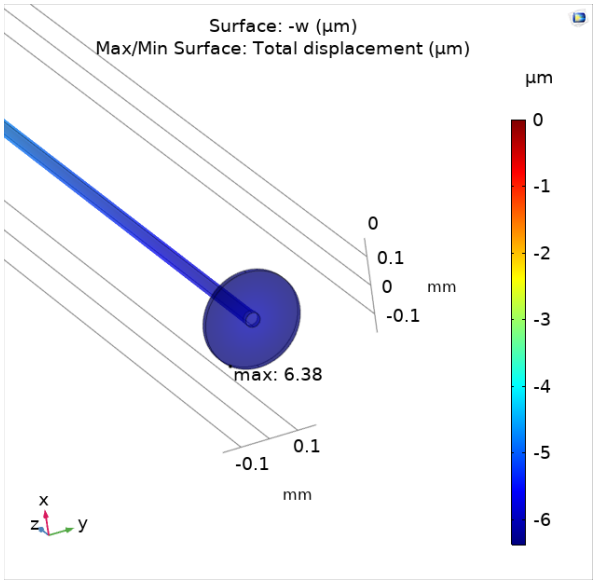

Figure 2-4: Simulation of the structural approach.

This result is validated in Comsol, using a simple model of the fiber and a rigid disk. The bellows were not considered as they are assumed to have zero stiffness. An image of the

simulation is seen in Figure 2-4. The value retrieved for strain in the fiber is $\epsilon_x = 0.596$ nanostrain Pa^{-1}.

2-2-2 Bending Approach

The bending approach is based on attaching a flexible beam to the fiber. When bending the fiber alone the strain in the center of the fiber is zero. This is due to the neutral bending axis is in the center of the fiber. When a flexible body is fixed to the fiber this neutral bending axis shifts away from the center of the fiber. This causes axial strain in the fiber when the total system is bent. An optimal case of this concept is shown in Figure 2-5.

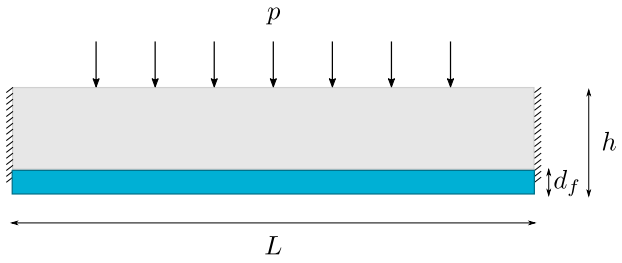

Figure 2-5: Schematic of the bending approach.

The maximum stress σ_{max} in the fiber is described in Equation 2-3 [13]

$$\sigma_{max} = \frac{Mc}{I} \tag{2-3}$$

M is the bending moment on the beam, c is the distance from the neutral bending axis and I is the moment of inertia of the cross sectional area. Combing $\epsilon_x = \sigma_x/E$ and $M = \frac{1}{2}FL$, where F is the force due to the pressure acting on the system with Equation 2-3, the strain is obtained as Equation 2-4.

$$\epsilon = \frac{FLc}{2IE} \tag{2-4}$$

For the performance estimation of this concept the system is assumed to have a rectangular cross section area and the moment of Inertia is $I = \frac{1}{12}bh^3$, where h is indicated in Figure 2-5 and b is the out of plane depth. The Young Modulus is calculated using Equation 2-5, which assumes the system as two parallel springs.

$$E_{tot} = \frac{E_{fiber}A_{fiber} + E_{polymer}A_{polymer}}{A_{tot}} \tag{2-5}$$

To get a realistic estimation of the pressure to strain conversion of this concept, the surrounding casing that is necessary for this concept to function is accounted for. This leads to the assumption that the dimensions h and b are 230 μm. Using the parameters $E_{polymer} = 0.1$ GPa, $E_{fiber} = 72$ GPa, $h_f = 50\mu$m and $L = 1$ mm, the strain at the edge of the system $c = \frac{1}{2}h$ is calculated. This results in an estimated maximum pressure to strain conversion of 10.8 nanostrain Pa^{-1}.

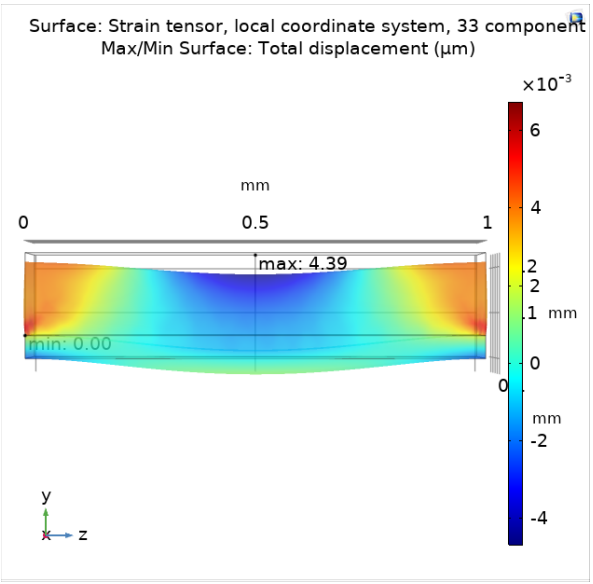

Figure 2-6: Simulation of the bending approach.

To verify these results a numerical model of this system has been composed in Comsol. An illustration of this model is shown in Figure 2-6. The resulting pressure to strain conversion is 1.17 nanostrain Pa^{-1}. This is significantly lower than the expectation from theory. The reason for this is the assumption made in retrieving the total Young Modulus E_{tot}, and assuming that the neutral bending axis is in the middle of the system. In reality this axis is closer to the stiffer body. A big advantage of the bending approach is that the pressure to strain conversion can be improved by increasing the length L. A disadvantage of this approach is that bending the fiber leads to a nonuniform strain profile.

2-2-3 Auxetic Metamaterial Approach

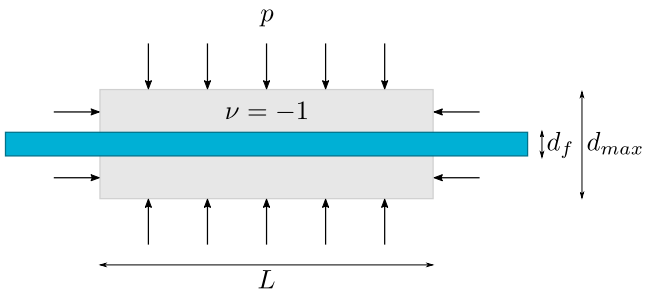

Figure 2-7: Schematic of the auxetic metamaterial approach.

An optimal case for the auxetic metamaterial approach consists of a fiber and a solid cylinder representing the auxetic coating. The axial strain ϵ_x caused by pressure p is calculated using Equation 2-6 from Lui et al. [14]. In this equation, E_{tot} is the lumped Young Modulus of the auxetic material and the fiber as in Equation 2-5. The Young Modulus for the auxetic material and the fiber are $E_{aux} = 0.1$ GPa, $E_{fiber} = 72$ GPa. Using the Diamters $d_{max} = 330$

μm, $d_f = 50$ μm results in a lumped Young Modulus of $E_{tot} = 1.75$ GPa. An isotropic Poisson ratio of $\nu = -1$ leads to an axial strain estimation of 1.71 nanostrain Pa^{-1}.

$$\epsilon_x = \frac{p}{E_{tot}}(1 - 2\nu) \tag{2-6}$$

A simulation of this system is performed in Comsol. The auxetic coating is considered as a solid with $E_{aux} = 0.1$ GPa and a Poisson ratio of $\nu = -0.99$. The dimensions of the system are the same as in the analytic estimation. Pressure was applied on the surface of the auxetic coating. The simulation is shown in Figure 2-8. The resulting axial strain in the fiber is 1.22 nanostrain Pa^{-1}.

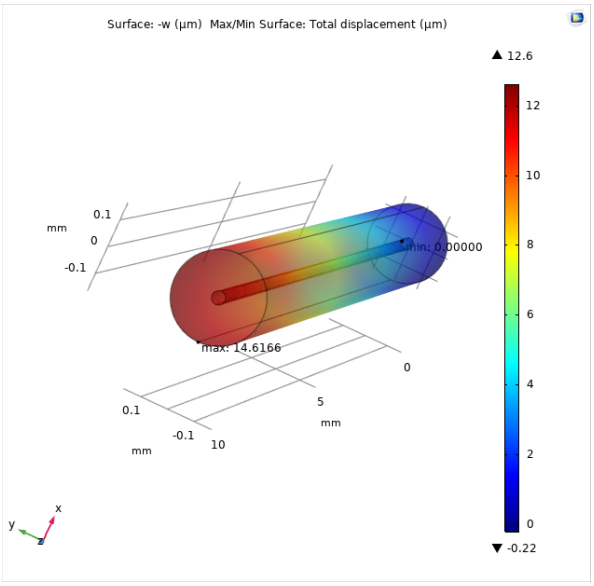

Figure 2-8: Simulation of the auxetic metamaterial approach.

2-3 Conclusion

In Table 2-1 an overview of the achievable pressure to strain conversion for the three optimal cases considered is shown. From considering the optimal case, where the auxetic metamaterial is simplified as solid, it has been shown that an approach with auxetic metamaterials is a promising solution direction to consider. The predicted maximum pressure to strain conversion of this approach is 1.22 nanostrain/Pa. Another advantage of the auxetic metamaterial approach over the bending approach is the expected linear relation between strain and pressure. The bending approach results in a nonuniform strain profile in the fiber, which makes it difficult to implement this approach into a sensor.

Approach	Schematic	Important Parameters	Axial Strain [nanostrain/Pa]
Auxetic Metamaterial	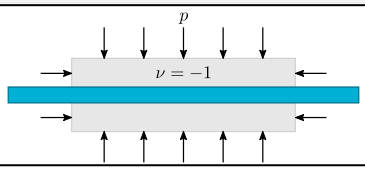	d_f, d_{max}	1.22
Structural	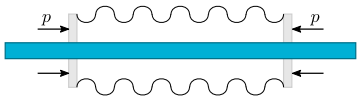	d_f, d_{max}	0.596
Bending	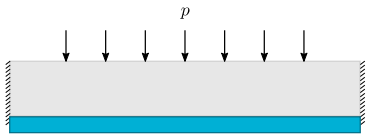	L, d_f, d_{max}	1.17

Table 2-1: Overview of achievable strain for different design approaches that follow from the FEM analysis. Additionally, the most important design parameters of the approaches are listed.

Chapter 3

Measuring The Poisson Ratio of 2D Auxetic Structures

Properties of Auxetic structures are designed using the mechanics of a unit-cell. The mechanics of different auxetic structure types found in literature are discussed in Appendix A. An assumption made in the theoretical models is that the unit-cell is surrounded by an infinite number of other unit-cells. In reality, a 2D auxetic metamaterial consists of a finite amount of unit cells. This introduces boundary effects and causes unit-cells throughout the structure to behave differently.

In this chapter, an experiment is presented to determine the effect of fixed and free boundary constraints that are introduced during compression tests. The goal of this experiment is to tell in which region of the auxetic structure it can be considered unconstrained, where there is no significant boundary effect on the auxetic behavior. This is useful for the verification of theoretical models of unit-cells.

A method to optically measure the displacement of a grid of pointers during deformation throughout a 2D structure, using a camera system, is presented. In the next part, the data resulting from the experiment is analyzed in different ways to retrieve the effective Poisson ratio. The reliability of the measurement method is considered, checking for sliding of the applied markers that are used to measure the displacements within the structure.

3-1 Methodology

In this section, the methodology to experimentally retrieve the effective Poisson ratio of auxetic 2D structures is presented.

3-1-1 Samples and Fabrication

For the experiment described in subsection 3-1-2 two types of structures are fabricated, see Figure 3-1. The isotropic Anti Tetra Chiral structure (Sample A.1) and the an-isotropic Meta Tetra Chiral structure (Sample A.2). Both structures have a high number of unit-cells. Using the analytical methods described in Appendix A, the structures are designed. The calculated properties are shown in Table 3-1.

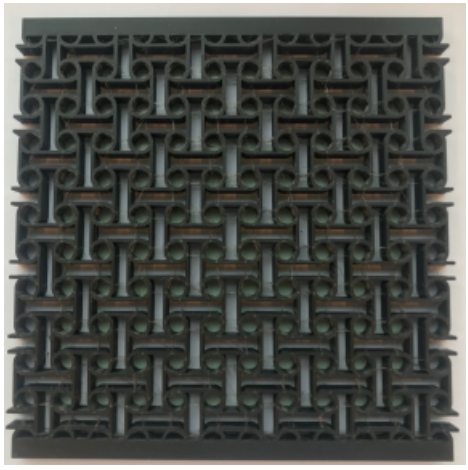

(a) Sample A.1, an Anti Tetra Chiral Structure of 10×12 unit-cells. The theoretical effective properties of a unit cell are $\nu_{yx} = -1$ and $E_x = E_y = 6.48$ MPa.

(b) Sample A.2, a Meta Tetra Chiral Structure of 10×14 unit-cells.The theoretical effective properties of a unit cell are $\nu_{yx} = -0.83$, $E_x = 5.78$ MPa, $E_y = 5.18$ MPa.

Figure 3-1: The structures and their effective properties used for the compression experiment. Geometrical details of the structures are listed in Appendix B. The material used is PET ($E = 1.85$ GPa).

Sample	Type	E_x [MPa]	E_y [MPa]	ν_{yx}	E_s [GPa]
A.1	Anti Tetra Chiral	6.48	6.48	-1	1.85
A.2	Meta Tetra Chiral	5.78	5.18	-0.83	1.85

Table 3-1: Overview of effective properties that follow from theory for a unit-cell. Effective Young moduli E_x and E_y. The effective Poisson ratio ν_{yx}, as defined in Equation 2-1 and the Young Modulus of the host material E_s.

For a complete overview of the geometric properties of the samples used in this research refer to Appendix B.

The structures are fabricated using a Prusa MK2 with PET-G filament. The effect of this manufacturing method on the material specifically for 2D auxetic structures is investigated in Appendix C. From this analysis it is concluded that the printed PET-G has an isotropic Young

Modulus of $E = 1.85$ GPa, and there is no dependency on printing direction, specifically when printing thin 2D beam structures.

3-1-2 Experimental Set-up

In Figure 3-2 the experimental configuration is shown. The sample is placed in a Zwick and Roell static material testing machine. A vertical displacement $u_y \approx -4$ mm is applied, compressing the sample. The compression cycle going from an undeformed state, to the maximum deformed state lasts 30 seconds.

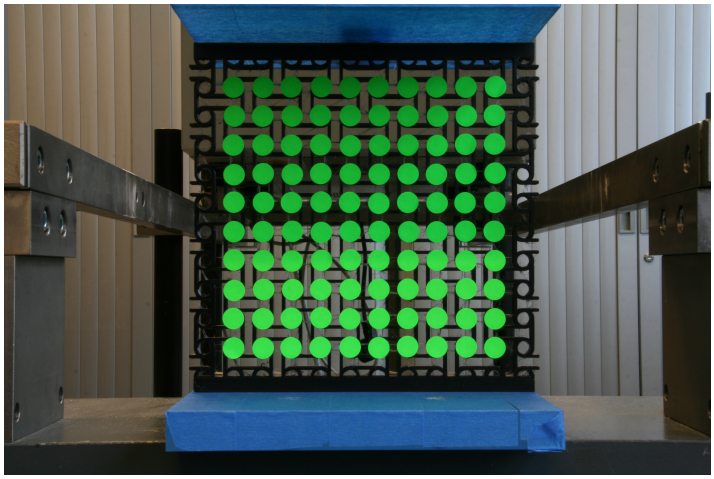

Figure 3-2: An image of the experimental configuration used to measure displacements throughout the plane. The sample is compressed in a Zwick & Roell machine. The location of a 10 x 10 Grid of green circular markers is captured by camera. This is *Sample A.1* an Anti Tetra Chiral structure.

With a Canon camera, which has a resolution of 2500×3500 pixels, 1 image per second is captured during the compression cycle. This process is repeated several times per structure. The markers are circular stickers and are positioned so that the circle centers overlaps with the centers of the chiral unit-cells. The use of markers and what this means for the measurement accuracy is discussed further in subsection 3-3-1.

3-1-3 Retrieving Displacements

The captured images are analyzed using the image processing toolbox from Matlab, which can recognize shapes like circles. A function was written that extracts and sorts the centers of the markers from the image, returning the x, y coordinates (in pixels) for the nodes. The script used is found in Appendix F.

In Figure 3-3 a snapshot of an analyzed image is shown. In this image 1 pixel corresponds to 0.11 mm. The region which is captured, or so called region of interest, determines this ratio. The image recognition software from Matlab uses values from multiple pixels (the circumference crosses more than $2\pi r = 370$ pixels) to retrieve the location of the circle

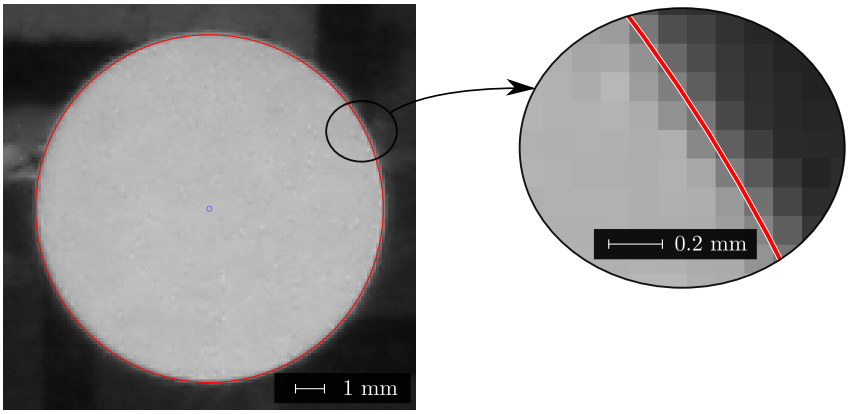

Figure 3-3

and is capable of determining sub pixel displacements. This reasoning leads to an estimated measurable displacement of 0.5 mm in the case of a region of interest covering all the markers.

Different ways of processing the data are discussed in depth in subsection 3-2-1 and subsection 3-2-2.

The choice for using markers was based on the finding that the circles, present in the geometry, were hard to track due to inconsistency in lighting.

3-1-4 FEM analysis

For verification purposes a FEM simulation is performed. The resulting deformed structures are seen in Figure 3-5. The FEM analysis of Sample A.1 and A.2 consist of a 2D model of the full structure, with a triangular mesh. A close up of a meshed unit-cell is shown in Figure 3-4.

(a) **(b)**

Figure 3-4: Meshes used for the simulation of Sample A.1(a) and A.2(b)

The bottom boundary has a fixed constraint and on the top boundary a prescribed vertical displacement u_y is applied. To see how the structure properties change for increasing strains, a parametric sweep for u_y is performed, while solving for geometric non linearity. The Poisson ratio is determined using the centers of solid circles in the middle of the structure.

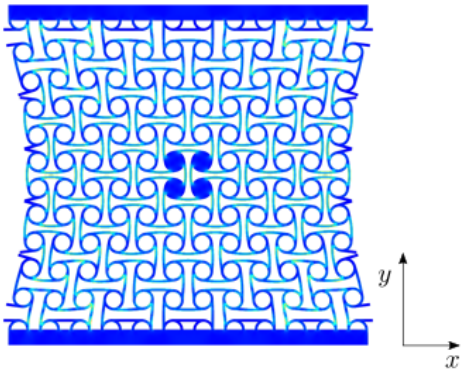

(a) Sample A.1, an Anti Tetra Chiral Structure of 10×12 unit-cells. The structure is loaded from $\epsilon_y = \{0.1\%, ..., 2.3\%\}$. This image is from the final load case, the scale factor for displacement is 3.

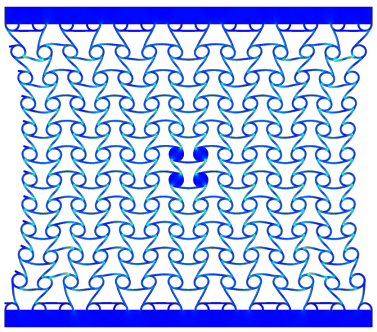

(b) Sample A.2, a Meta Tetra Chiral Structure of 10×14 unit-cells. The structure is loaded from $\epsilon_y = \{0.1\%, ..., 2.41\%\}$. This image is from the final load case, the scale factor for displacement is 3.

Figure 3-5: Resulting displacement and von Mises stress from simulation for Sample A.1 and A.2

3-2 Data Analysis

This section discusses how the acquired data from the experiment is analyzed. First, a method that uses rectangular planes is presented. Second, the Poisson ratio per unit-cell is considered. Finally the Poisson ratio versus strain is retrieved and compared for the two samples.

3-2-1 Calculating Poisson with Rectangular Planes

Alomarah et al. [15] present a method to experimentally retrieve the Poisson ratio, ν_{yx}. This method uses the definition of a plane inside the structure where the Poisson ratio is assumed to be uniform. The deformation of this plane is retrieved by tracking the displacement of 8 points in the structure. The deformation of the plane is constructed using the average of the y displacement of the yellow nodes and the average x displacement of the blue nodes.

The choice for the location of the plane is not elaborated on. Alomarah et al. do notice the effect of the boundaries of the plane as they make an effort to reduce the effects with hinges and lubrication. However there is still a considerable nonuniform displacement noticeable in x in Figure 3-6.

In this section, using the concept of a plane as Alomarah et al. described, it is investigated how positioning of the corner-nodes of a plane effects the measured Poisson ratio.

Figure 3-7 illustrates the definition of the location of the plane. The position of the plane is defined by m, as the distance from the fixed boundaries, and n, as the distance from the free boundaries. The plane is symmetric along the same symmetry axis as the auxetic structure. The plane has dimensions L_x and L_y, which are calculated with Equation 3-1, using the x, y coordinates of the nodes $\{1, .., 4\}$ indicated in blue in Figure 3-7.

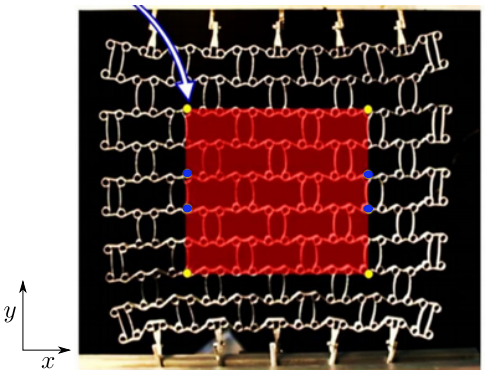

Figure 3-6: Experimental method of Alomarah et al. [15], consisting of 8 data points, where the x displacement in the auxetic structure is calculated by taking the average of the blue nodes. The y displacement is retrieved from the yellow nodes.

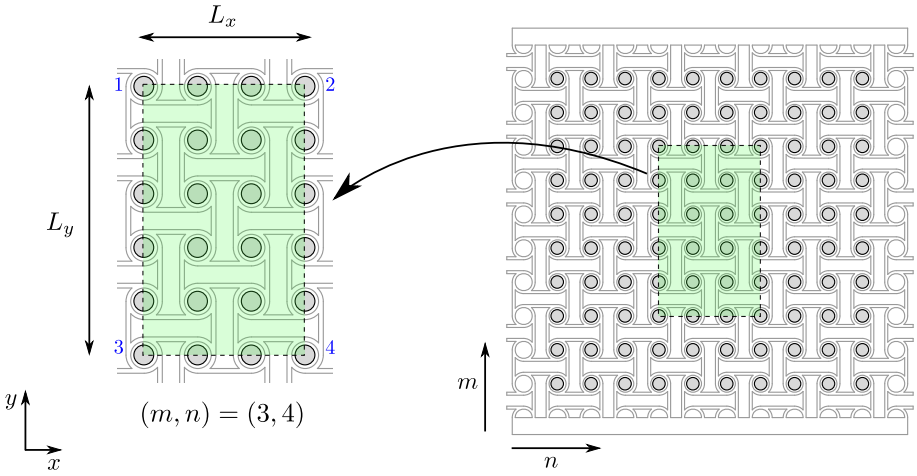

Figure 3-7: A Schematic of the marker grid for Sample A.1. m indicates the vertical distance in nodes from the fixed boundary, n indicates the horizontal distance in nodes from the free boundary. Together m and n define a rectangle and the 4 nodes that are used in the calculation of ν_{yx}. The planes symmetry axes always coincide with the symmetry axes of the structure.

$$\begin{aligned} L_x &= \frac{1}{2}(x_1 + x_3) - \frac{1}{2}(x_2 + x_4) \\ L_y &= \frac{1}{2}(y_1 + y_2) - \frac{1}{2}(y_3 + y_4) \end{aligned} \tag{3-1}$$

The changes in lengths caused by displacement are retrieved in Equation 3-2.

$$\begin{aligned} \delta_x &= L_{x1} - L_{x0} \\ \delta_y &= L_{y1} - L_{y0} \end{aligned} \tag{3-2}$$

Where L_{x1} and L_{x0} are the lengths of loaded and unloaded frame respectively. The strains are defined as by $\epsilon_x = \delta_x / L_x$. Finally, the Poisson ratio of the plane is calculated in Equation 3-3.

$$\nu_{yx} = -\frac{\epsilon_x}{\epsilon_y} \tag{3-3}$$

The undeformed frame ($\epsilon_y = 0\%$) and the maximum deformed frame ($\epsilon_y \approx 2\%$) are compared for several deformation cycles for both Sample A.1 and A.2. The resulting ν_{yx} is plotted in Figure 3-8 and Figure 3-9 for the different planes indicated by m and n.

Increasing the distance from the fixed boundary, results in a measured ν_{yx} closer to the theoretical value for which the structure is designed. In the right plot of Figure 3-8, ν_{yx}

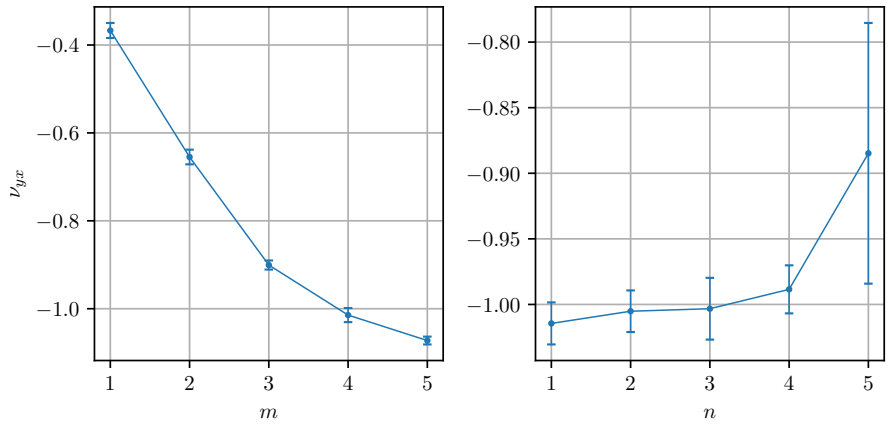

Figure 3-8: Results for the Anti-Tetra Chiral Structure (Sample A.1). The experiment is repeated 7 times. The average Poisson ratio is plotted against the different corner nodes of the rectangle, described in Figure 3-7. For the left plot, the distance (m) from the fixed boundary is varied while keeping $n = 1$. For the right plot the distance n from the free boundary is varied while keeping $m = 4$.

is plotted for increasing n, while keeping m constant at 4. When n is 5 the value starts to deviate from the predicted value. A possible reason for this that the measurable displacements decrease. When the applied strain is $\epsilon_y = 2\%$ and the plane is defined as $(m, n) = (5, 5)$ it measures 25×25 mm. The displacement of this plane is $\delta_y = 25 * \epsilon_y = 0.5$ mm. This approaches the estimated measurable displacement of 0.05 mm, as discussed in section 3-1, and leads to measurement inaccuracy.

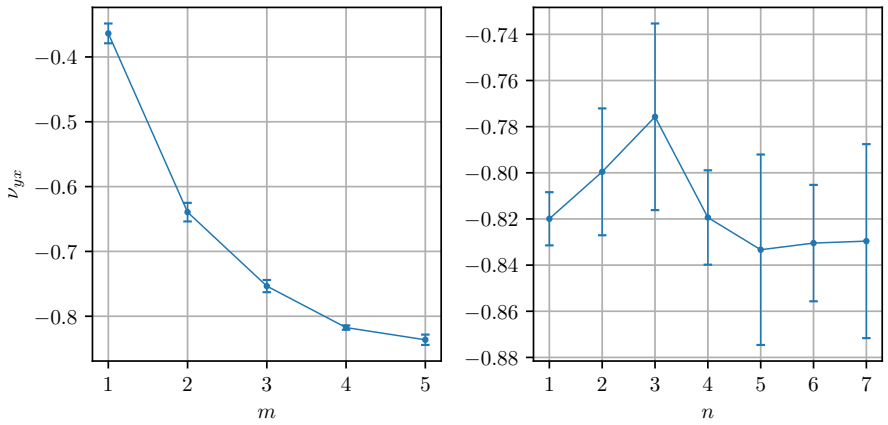

Figure 3-9: Results for the Combi-Tetra Chiral Structure (Sample A.2). The experiment is repeated 5 times. The average Poisson ratio is plotted against the different corner nodes of the rectangle, described in Figure 3-7. For the left plot, the distance (m) from the fixed boundary is varied while keeping $n = 1$. For the right plot the distance n from the free boundary is varied while keeping $m = 4$.

3-2-2 Poisson ratio per Unit-Cell

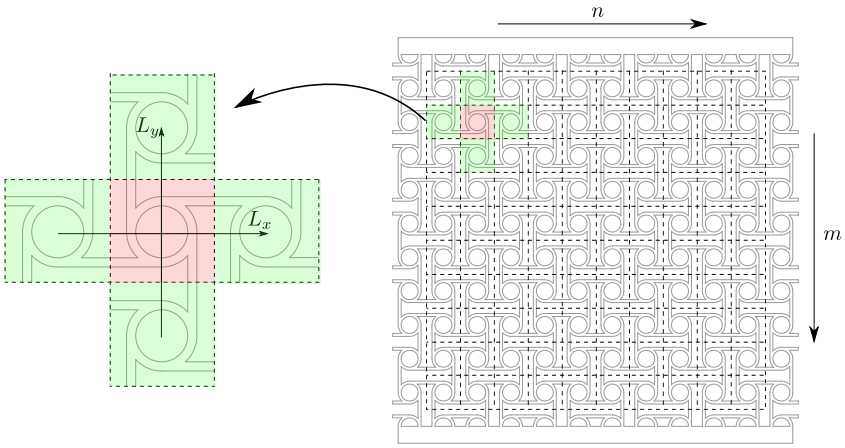

Figure 3-10: Definition of unit-cells in the Anti Tetra Chiral structure. The unit-cell indicated in red, is calculated using the distance of the surrounding markers indicated in green. For the calculation of the boundary and corner unit-cells refer to Appendix D

From the previous section it follows that measurement location is very important when determining the Poisson ratio. To get a better insight in the effect of the fixed boundary on the auxeticity of the structure, the Poisson ratio for individual unit-cells is investigated. The definition of a unit-cell and the displacements used to calculate the Poisson ratio is illustrated in Figure 3-10. The calculation for the unit-cell, indicated in red, uses the coordinates of the surrounding green unit-cells. The full calculations are found in Appendix D.

In Figure 3-11 and Figure 3-12, ν_{yx} is plotted for every unit-cell. The difference with the value from theory is high at the fixed boundaries, as expected. Further from the boundary,

the measured ν_{yx} starts to approach the theoretical value for a unit-cell .

For Sample A.1, the unit-cells on free boundaries $(m, n) = (1, 6)$ and $(m, n) = (10, 6)$ have a $\nu_{yx} < -1$. This means the unit-cell is more auxetic than theory. This is in conformation with Figure 3-5a, where the unit-cells in the middle of the free boundaries rotate more than other unit-cells because the horizontal bars touch. This same effect is also visible in Figure 3-8 where $\nu_{yx} < -1$ for $m = 4$ and $m = 5$ at the free boundary.

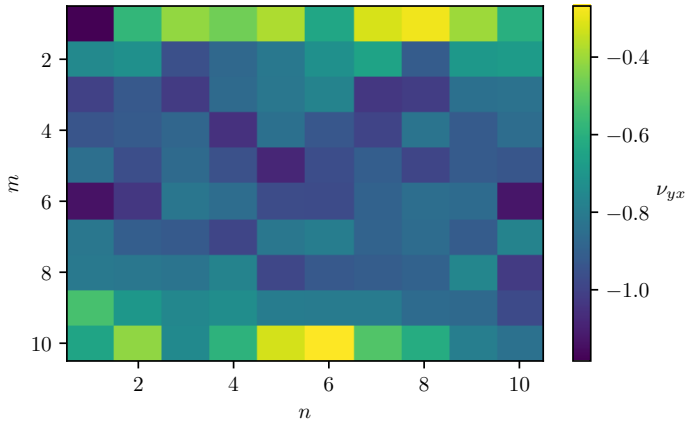

Figure 3-11: A plot of e_ν as the difference between the theoretical Poisson Ratio of $\nu_{yx} = -1$ and the data from the experiment for every unit-cell of Sample 1.A. This is for $\epsilon_y \approx 2\%$.

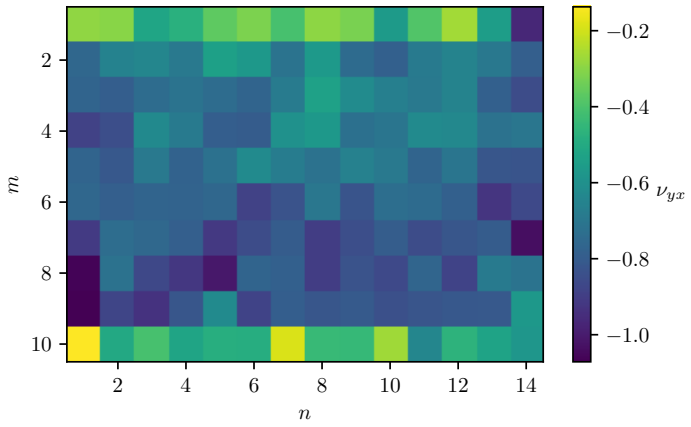

Figure 3-12: A plot of e_ν as the difference between the theoretical Poisson Ratio of $\nu_{yx} = -0.83$ and the data from the experiment for every unit-cell of Sample 2.A. This is for $\epsilon_y \approx 2\%$.

In order to compare the method using rectangular planes described in subsection 3-2-1 with calculation of the Poisson ratio per unit-cell, the data is plotted as in Figure 3-14 and 3-13 for varying the distance from the fixed boundary (m) and varying the distance from the free boundary (n). The result in shown in Figure 3-14 and 3-13 for Sample A.1. For Sample A.2 The result is plotted in Figure 3-16 and 3-15. The standard deviation of the measurements per unit-cell is significantly higher than for measuring with rectangular planes. However, similar large deviations from the theoretical Poisson ratio are seen close to the fixed boundaries both for Sample A.1 and Sample A.2.

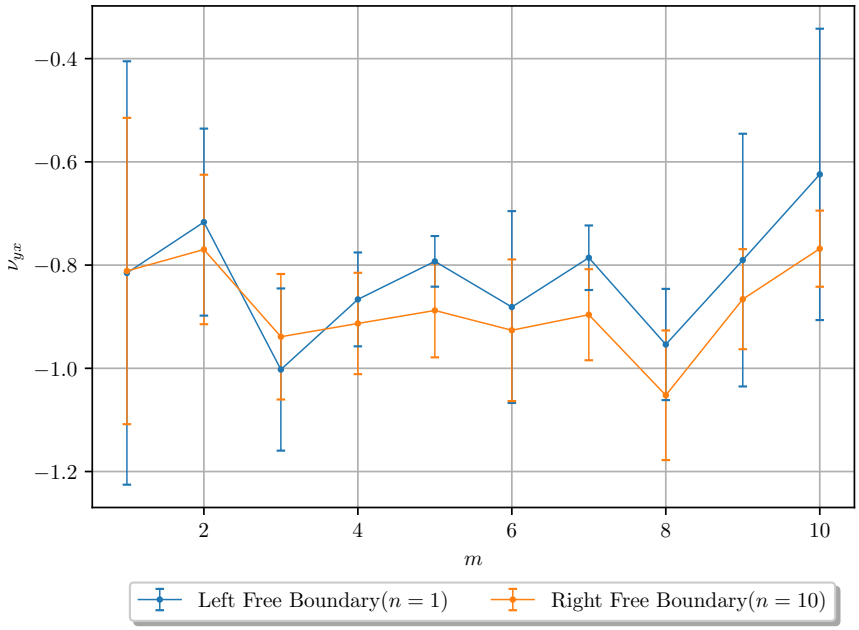

Figure 3-13: Results for the Anti Tetra Chiral structure. The Poisson ratio, ν_{yx}, is calculated per unit-cell.

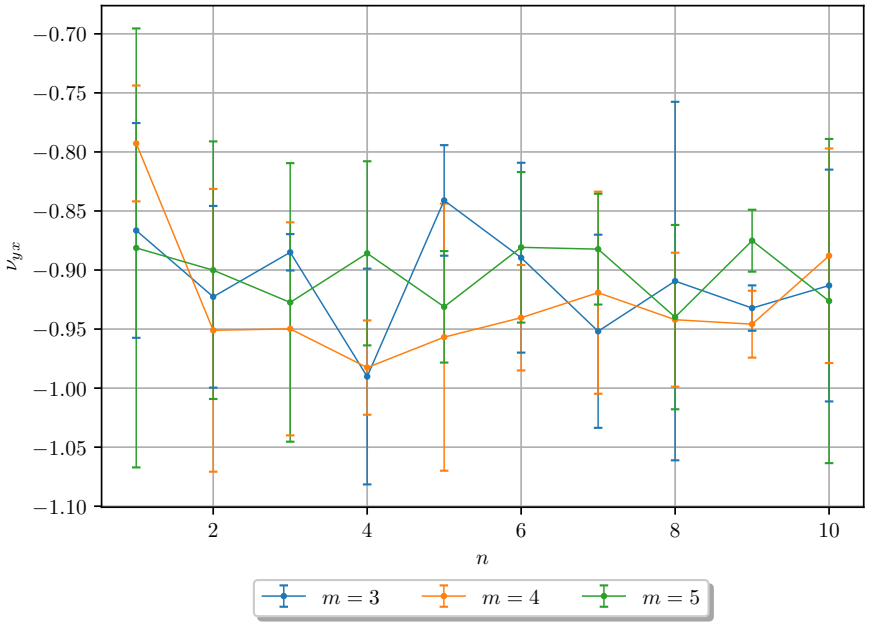

Figure 3-14: Results for the Anti Tetra Chiral structure. The Poisson ratio, ν_{yx}, is calculated per unit-cell.

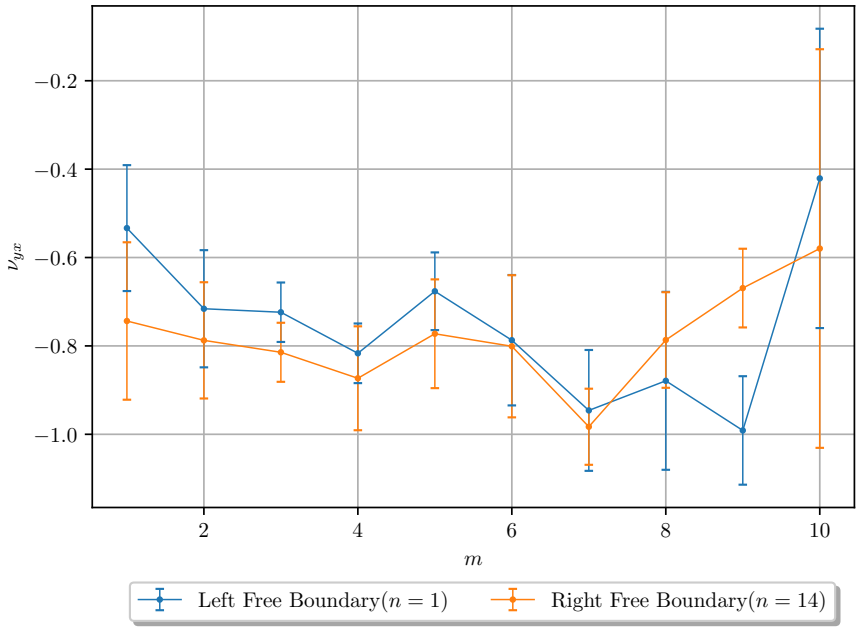

Figure 3-15: Results for the Meta Tetra Chiral structure. The Poisson ratio, ν_{yx}, is calculated per unit-cell.

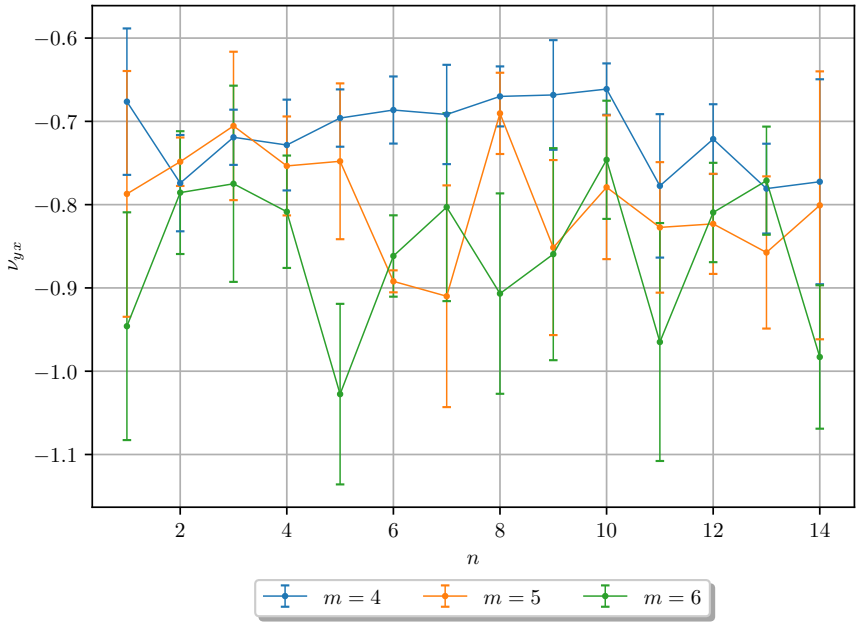

Figure 3-16: Results for the Meta Tetra Chiral structure. The Poisson ratio, ν_{yx}, is calculated per unit-cell.

3-2-3 Poisson ratio versus strain

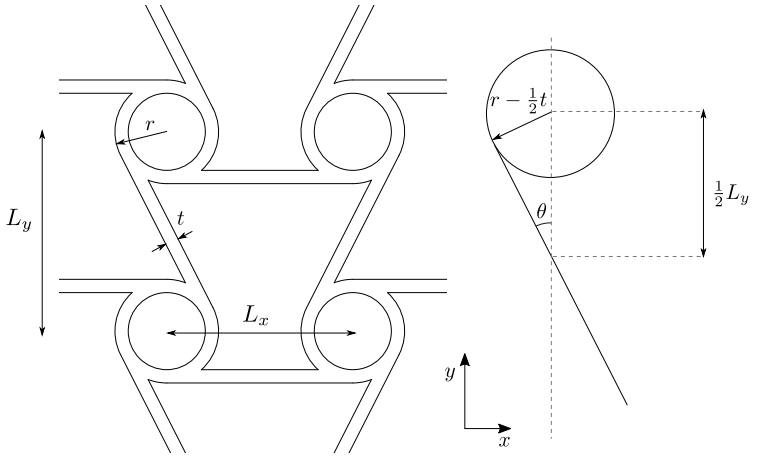

Figure 3-17: Schematic of a Meta-Chiral Structure as described by [16]

From theory the Anti Tetra Chiral structure is expected to have a constant ν_{yx} for increasing strain, because the structure is symmetric. For a Meta Tetra Chiral structure the Poisson ratio is dependent on θ and is defined as,

$$\nu_{yx} = -(L_y/L_x)\cos(\theta) \tag{3-4}$$

The parameters of this equation are indicated in Figure 3-17. The derivation of the Poisson ratio and other details on the theoretical model are discussed in Appendix A. When the structure is compressed θ increases and $\cos(\theta)$ decreases, this leads to a decreasing ν_{yx}.

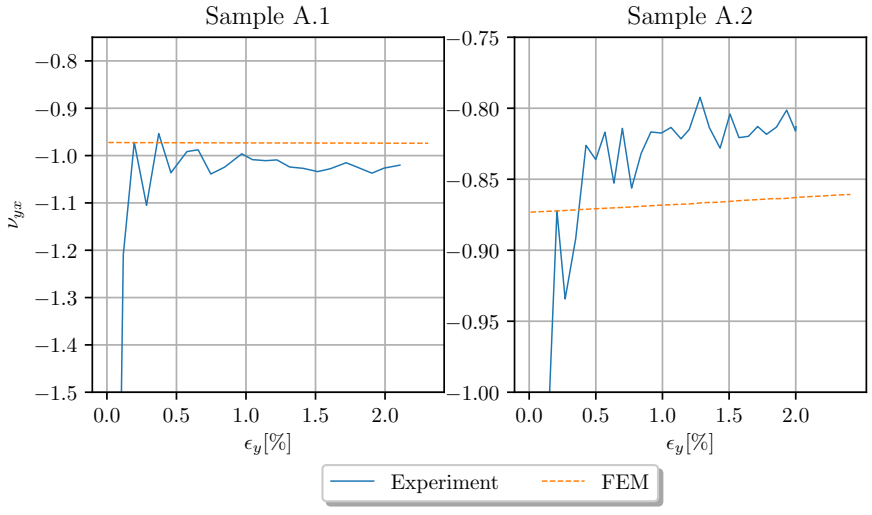

Figure 3-18: The Poisson ratio is plotted versus strain. ν_{yx} is measured at the plane of $m = 4$ and $n = 2$ for both samples A.1 and A.2.

In Figure 3-18 ν_{yx} is plotted against the vertical strain ϵ_y. After a disturbance for small strains, which is caused by measurement inaccuracy, it settles to one value. From the experimental

data it is hard to verify the decreasing Poisson ratio for Sample A.2. The results from the FEM model show a constant ν_{yx} for Sample A.1. For Sample A.2 a clear decrease in ν_{yx} is noticed.

3-3 Discussion of Results

The results from measuring with rectangular planes show a small standard deviation of the retrieved effective Poisson ratio. When the distance m from the fixed boundary increases, the retrieved Poisson ratio approaches the theoretical Poisson ratio.

For $m = 5$, in both samples the measured Poisson ratio overshoots the theoretical value due to the free boundary. The effect of the free boundary dissipates fast in Figure 3-8, but for $n = 4$ the Poisson starts increase. This effect is not expected, but is explainable by increasing measurement accuracy when the size of the rectangular plane decreases.

Looking at the displacements of every individual unit cell, similar results are seen as with the method using rectangular planes. Unit-cells close to a fixed boundary, have a strong deviation from the theoretical value. For calculation of the Poisson Ratio per unit cell the displacements δL_i between loaded and unloaded frames are in the order of 0.1 mm. This explains the fluctuation of e_ν seen in Figure 3-11 and Figure 3-12. From the standard deviations seen in Figure 3-14,3-13,3-16 and 3-15, the lack of measurement accuracy is also seen. To improve accuracy and keep all the unit-cells in the picture frame, a camera with a higher resolution is needed.

The results in Figure 3-18 for show a similar trend for values from the FEM analyses and experiment for both samples. The experimental data shows a rise time for small strains, which is explainable by the accuracy limit of the measurement method.

3-3-1 Measuring with Markers

In the experiment multiple compression cycles have been done. During a cycle, images have been captured continuously. In the first image, the structure is not deformed. The marker positions in the first image of every cycle are compared. A difference in coordinates between the first images means there is movement. This can be movement of the camera, lens or a shift of the markers.

A total of 5 compression cycles are considered. The unloaded image of the first cycle is taken as a reference. The difference between the reference image and the unloaded image of cycles $\{2, .., 5\}$ is plotted in Figure 3-19. The red vectors indicate the displacement direction. For visibility purposes, the vector amplitude is scaled. The actual maximum vector length is 5.4056 pixels $\approx$ 0.6 mm.

If the camera only translates, this results in a field of parallel vectors. If the image scales, due to auto-zoom, this results in vectors with a similar direction. However, the length of the vectors is dependent on the location of the focus point. Vectors close to the focus point are small, vectors further away from the focus point are large. This effect is seen in Figure 3-19. The shifting of a marker sticker leads to a vector with a different length and direction than the rest of the vectors. As the vectors are all pointing in a similar direction the markers have

not shifted. It is concluded that a slight camera and lens movement caused the picture frame between different deformation cycles to shift a maximum of 0.6 mm. The auto-zoom only adjusted the lens for the first image of a cycle, so this does not affect the measurement. The movement of the camera does not affect the calculation of the Poisson ratio, as it does not affect the ratio of the distances between the markers.

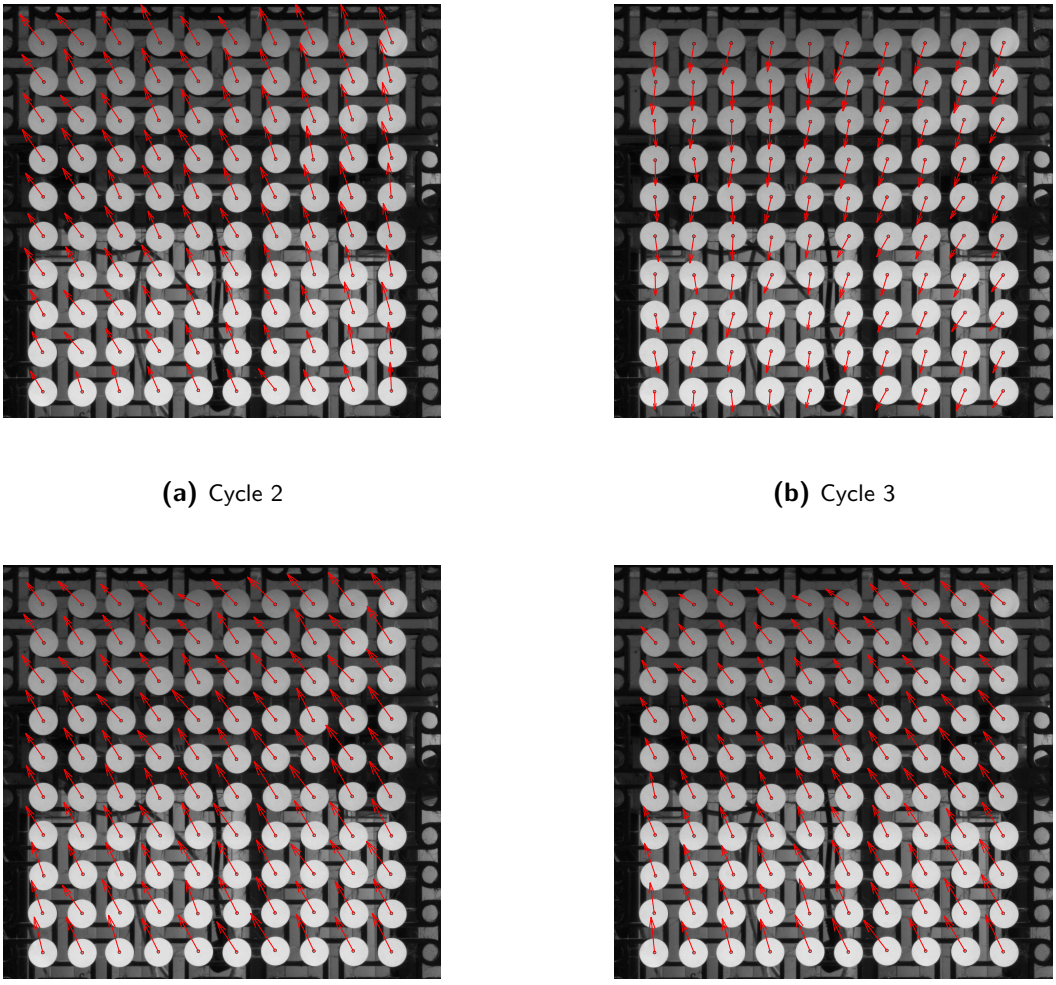

(a) Cycle 2 **(b)** Cycle 3

(c) Cycle 4 **(d)** Cycle 5

Figure 3-19: Vectors indicating the difference between the reference image, and the first images of cycles $\{2, .., 5\}$. The vectors are scaled, the maximum absolute displacement is 5.4056 pixels.

3-4 Conclusion

It is concluded that both the fixed as well as the free boundary affect the measurement of the Poisson ratio. The structure starts to behave more similar to theory further away from the boundaries. In the case of Sample A.1, for a measurement plane indicated with relative

distances from the boundaries $m = 4$ and $n = 3$, the calculated Poisson approaches the theoretical value. For Sample A.2 a similar trend is found.

From investigating the Poisson ratio per unit-cell, it has been shown that the unit-cells close to the boundary behave less auxetic. The measurement accuracy proved insufficient for determining the Poisson ratio per unit-cell, this is concluded from the high standard deviations in Figure 3-14.

From the FEM model as well as the experimental results, it is found that for an-isotropic auxetic structure (Sample A.2) the Poisson ratio is dependent on the applied strain. For symmetric structures as the Anti Tetra Chiral structure (Sample A.1) it is not dependent on strain. This confirmed the expectations from theory, as the ν_{yx} is dependent on the angle θ for Sample A.2. This angle changes when the structure is deformed. In general, strain dependency of the Poisson ratio for any auxetic structure type is predictable from the theory described in Appendix A. For example, it is expected that re-entrant honeycombs and Tri-Chiral structures have strain dependent Poisson ratios.

Chapter 4

Force Transmission in Auxetic Materials

In the this chapter the relation between the effective properties of an auxetic metamaterial and the ability to create strain in a body of another material is described. Making a design assumption, the auxetic structure is considered as a interface for force transmission or a *'gearbox'*. On the basis of this relation and the achievable effective properties for different auxetic metamaterial archetypes, which are described in Appendix A, a suitable structure type is chosen. To verify the expectations for the force transmission, one structure type is considered. The effect of changing the geometric parameters of this structure type, resulting in different effective material properties, is theoretically investigated. A selection of auxetic structure geometries is fabricated and an experimental setup is constructed to measure the force transmission for these structures. The results from this experiment are discussed and compared to the expectations. Next, using the verified model for force transmission, a second design iteration is performed to achieve high force transmission. Finally, a conclusion is drawn on the insights and results from investigating the designing, fabrication and testing of auxetic metamaterials for force transmission.

4-1 Defining Force Transmission

To create axial strain in a fiber an axial force has to be generated. Two designs concepts are considered. In the first concept (Figure 4-1a), the auxetic metamaterial is directly fixed to the optical fiber and the axial force is generated by shear on the boundary between the fiber and the auxetic structure. In the second concept (Figure 4-1b), the auxetic metamaterial is fixed to stiff end plates, which are connected to the optical fiber. The auxetic metamaterial is not fixed to the fiber itself, but it is in contact with the fiber.

(a) Concept 1 **(b)** Concept 2

Figure 4-1: Two potential design concepts using an auxetic metamaterial to convert pressure to strain. (a) The auxetic material is fixed to *'the fiber'*.(b) the auxetic material is fixed to *'solid end plates'* which transmit the force to the fiber.

In chapter 3, it has been shown that fixed boundaries have a significant effect on the behavior of auxetic structures. Additionally, the connection between the auxetic material and another solid material, i.e. the fiber, consists of thin beams with a small contact area. In order to show the difference between the concepts, two archetypes and their connection to the fiber or to the stiff end plates are illustrated in Figure 4-2. In concept 1 (Figure 4-2a), the strain transfer between the auxetic metamaterial and the fiber is mostly dependent on the bending of the ligaments. In concept 2 (Figure 4-2b), axial strain in the fiber is caused by a stretching load on the ligaments connected to the stiff end plates.

It is expected that concept 1 will perform less than concept 2, due to the difference in loading of the ligaments (bending versus stretching).

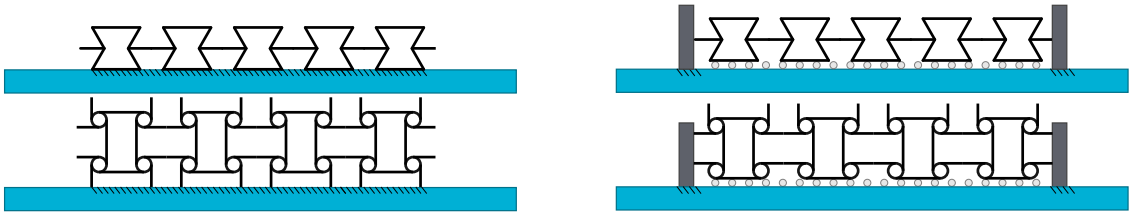

(a) Concept 1 **(b)** Concept 2

Figure 4-2: A snapshot of the boundary surfaces, for two archetypes of auxetic structures for both design concepts. In *(a)*, the strain in the fiber is caused through bending of the ligaments. In *(b)*, the axial strain in the fiber is caused by ligaments 'pulling' on the stiff end disk.

In this chapter the concept that uses two stiff end plates is considered. In this case a high force transmission from F_y, generated by the outside pressure to F_x contracting the disks

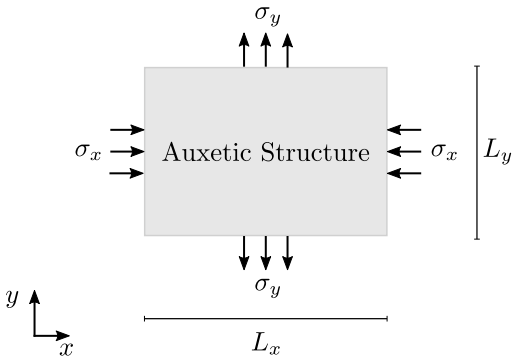

Figure 4-3: Schematic of the simplified system, used to estimate the force transmission in an auxetic metamaterial. σ_y is the reaction to the pressure that acts on the top boundary. σ_x is the stress caused by constraining the movement in x.

is desired. The ratio of F_x/F_y achievable by the auxetic material is used to indicate it's feasibility.

To compose the model for force transmission, the system is simplified to the free body diagram seen in Figure 4-3. The system is a 2D rectangular auxetic plate, consisting of multiple unit-cells. The amount of unit-cells and the geometry of a unit-cell determines dimensions L_x and L_y. It is assumed that the plate has the an-isotropic effective properties (ν_{xy}, ν_{yx}, E_x and E_y), that follow from the mechanics of the unit cell as described in Appendix A. The linear elastic deformation of the 2D system is described by Equation 4-1. To solve this equation it is assumed that the strains ϵ_x and ϵ_y are infinitesimally small.

$$\begin{bmatrix} \epsilon_x \\ \epsilon_y \\ \gamma_{xy} \end{bmatrix} = \begin{bmatrix} 1/E_x & -\nu_{yx}/E_y & 0 \\ -\nu_{xy}/E_x & 1/E_y & 0 \\ 0 & 0 & 1/G \end{bmatrix} \begin{bmatrix} \sigma_x \\ \sigma_y \\ \tau_{xy} \end{bmatrix} \tag{4-1}$$

A pressure in y is applied, this results in stresses σ_x and σ_y. Stress relates to force as $F = \sigma/\text{Area}$. Using the dimensions of the system and solving Equation 4-1, the force ratio (F_x/F_y) is retrieved as in Equation 4-2.

$$\frac{F_x}{F_y} = \frac{\sigma_x L_y}{\sigma_y L_x} = \left[\frac{L_y}{L_x}\right] \frac{E_x}{E_y} \nu_{yx} \tag{4-2}$$

First, the suitability for high force transmission of different auxetic structure types is investigated by considering a single unit-cell. When reviewing the theoretical models that are described in Appendix A, and using them in Equation 4-2, two structure types stand out. The Re-entrant Honeycomb structure and the Meta Tetra Chiral structure. Both have an-isotropic effective properties, which is important to be able to achieve high ratios of F_x/F_y. The other structures discussed in Appendix A are less suitable, as they are isotropic. This leads to a maximum force transmission of -1, for example for the Anti Tetra Chiral structure where $\nu_{yx} = -1$ and $E_x = E_y$.

Considering Figure 4-4 and 4-5 it is expected that high force transmission is achievable with a Re-entrant Honeycomb. The design parameters used for this initial evaluation are similar to

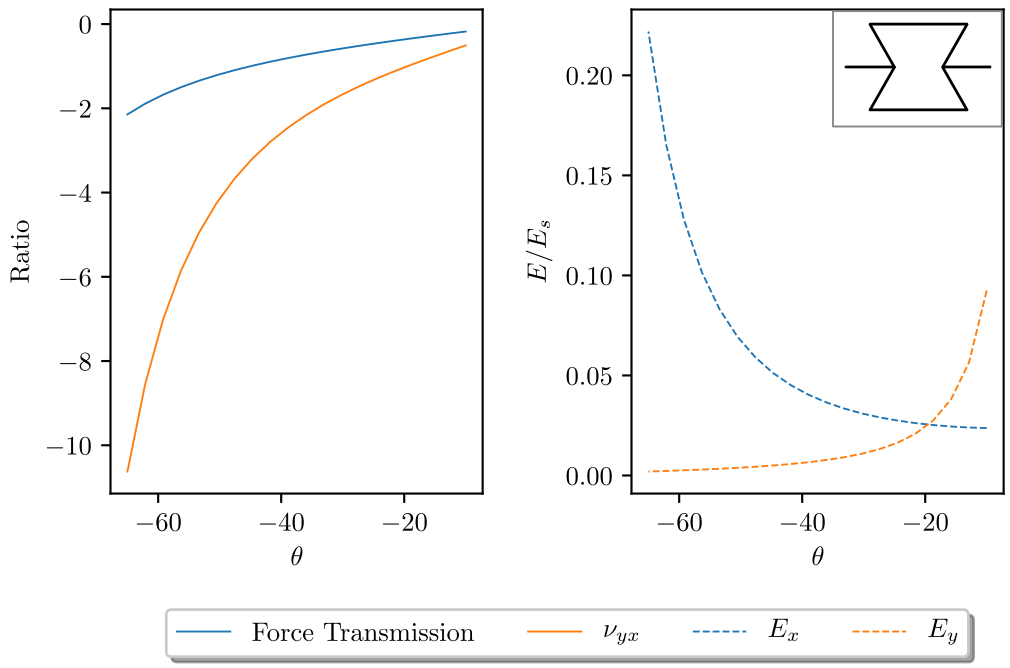

Figure 4-4: Force Transmission, Poisson ratio and the Young Moduli for a Re-entrant Honeycomb unit-cell. The geometric parameters used are $l = 5$ mm,$h = 15$ mm, $t = 1$ mm, $b = 1$ mm.

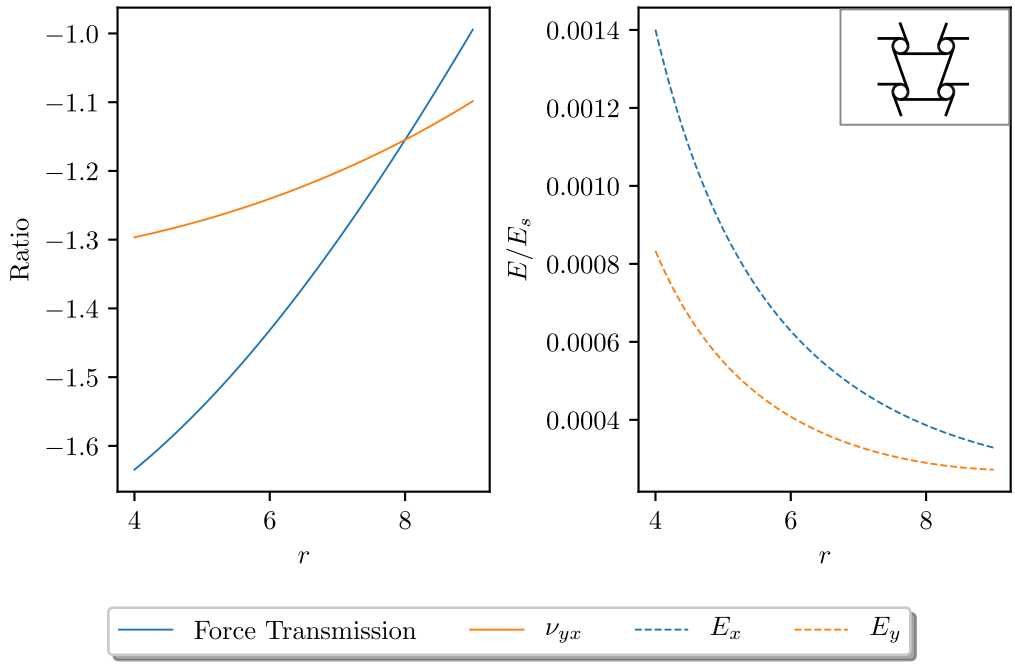

Figure 4-5: Force Transmission, Poisson ratio and the Young Moduli for a Meta Chiral Structure unit-cell. The geometric parameters used are $t = 1$ mm, $L_x = 40$ mm,$L_y = 30$ mm.

the examples found in literature of a typical Re-entrant Honeycomb structure [17] and a Meta Tetra Chiral structure [16]. Besides the effective properties of a unit-cell the force transmission is dependent on L_x and L_y. This means that the force transmission for a complete auxetic metamaterial is different than for a single unit-cell.

4-1-1 Force Transmission in Re-entrant Honeycombs

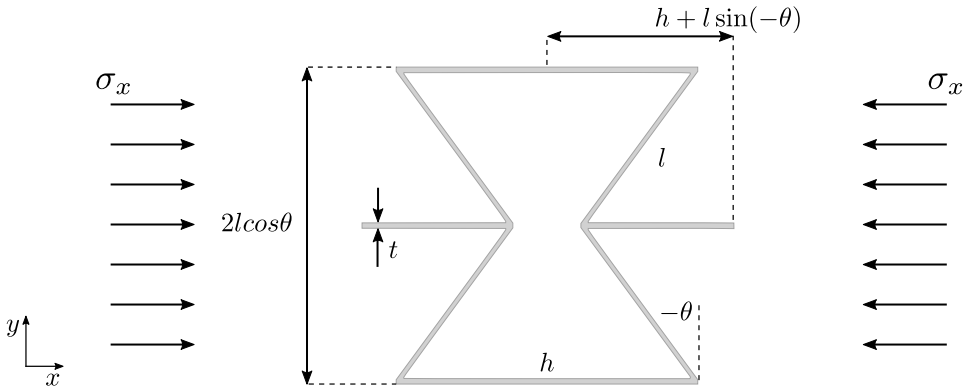

Figure 4-6: Dimensions of a Re-entrant Honeycomb

To further understand the force transmission behavior of the Re-entrant Honeycomb the theory that describes the effective properties is considered. Gibson and Ashby [18] present a flexure based model, as in Equation 4-5, to describe the effective an-isotropic properties ν_{xy}, ν_{yx}, E_x and E_y. The geometric parameters are shown in Figure 4-6. The deflection δ caused by flexure is related to force with the force constant K_f,

$$F = K_f \delta \tag{4-3}$$

The force constant K_f is defined as Equation 4-4 with beam thickness t, beam length l, the Young Modulus of the host material E_s and b is the out of plane depth.

$$K_f = \frac{E_s b t^3}{l^3} \tag{4-4}$$

The full derivation of these equations is considered in Appendix A. In this chapter the resulting equations for the effective properties are investigated to see what design parameters are influencing the force transmission.

$$\begin{aligned} E_x &= K_f \frac{h/l + \sin\theta}{b\cos^3\theta} \\ E_y &= K_f \frac{\cos\theta}{b(h/l + \sin\theta)\sin^2\theta} \\ \nu_{yx} &= \frac{\cos^2\theta}{(h/l + \sin\theta)\sin\theta} \\ \nu_{xy} &= \frac{(h/l + \sin\theta)\sin\theta}{\cos^2\theta} \end{aligned} \tag{4-5}$$

Besides flexure, shear and strain start to significantly contribute to the structure behavior when the geometry deviates from the 'standard' geometry with thin long beams. Gibsons model was expanded by Masters and Evans [17], to take these effects into account. The force constant K_h for shearing is defined in Equation 4-6, where G_s shear modulus of the host material. The geometric parameters that are used in Masters and Evans model are the same as before and are illustrated in Figure 4-6.

$$K_h = \frac{G_s bt}{l} \tag{4-6}$$

Similarly, the force constant for straining K_s is defined as Equation 4-7.

$$K_s = \frac{E_s bt}{l} \tag{4-7}$$

Combining the deformations caused by all three mechanisms, flexure, shear and strain, the effective properties of the Re-entrant Honeycomb are defined as in Equation 4-8. For the full derivation of these equations refer to [17].

$$\begin{aligned}
E_x &= \frac{1}{\frac{b\cos\theta}{h/l+\sin\theta}\left[\frac{\cos^2\theta}{K_f}+\frac{\cos^2\theta}{K_h}+\frac{2h/l+\sin^2\theta}{K_s}\right]} \\
E_y &= \frac{1}{b(h/l+\sin\theta)\left[\frac{\sin^2\theta}{K_f\cos\theta}+\frac{\sin^2\theta}{K_h\cos\theta}+\frac{\cos\theta}{K_s}\right]} \\
\nu_{xy} &= -\sin\theta(h/l+\sin\theta)\left[\frac{-\frac{1}{K_f}-\frac{1}{K_h}+\frac{1}{K_s}}{\left[\frac{\cos\theta^2}{K_f}+\frac{\cos^2\theta}{K_h}+\frac{2h/l+\sin^2\theta}{K_s}\right]}\right] \\
\nu_{yx} &= \frac{-\sin\theta\cos\theta\left[\frac{1}{K_f}+\frac{1}{K_h}-\frac{1}{K_s}\right]}{(h/l+\sin\theta)\left[\frac{\sin^2\theta}{K_f\cos\theta}+\frac{\sin^2\theta}{K_h\cos\theta}+\frac{\cos\theta}{K_s}\right]}
\end{aligned} \tag{4-8}$$

Difference between Models

From considering the force constants in Equation 4-4, 4-6 and 4-7, it is concluded that t/l determines the magnitude of the force constants which is directly related to the contribution of each mechanism. In Equation 4-8 a small force constant relates to a high contribution of the to the effective properties. K_f scales with $(t/l)^3$ while K_h and K_s scale with (t/l).

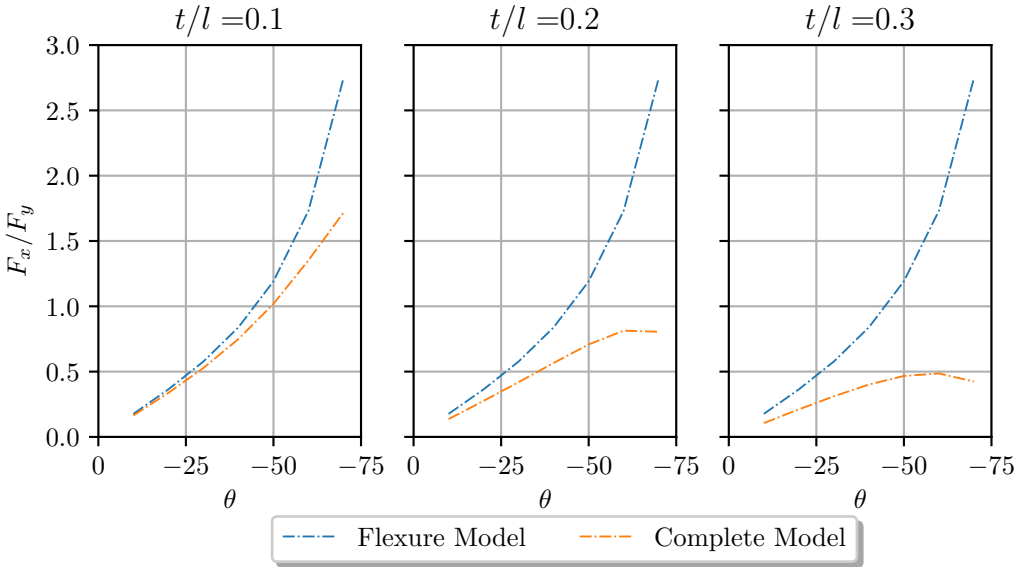

Figure 4-7: Comparison of the two models for force transmission, for varying t. Values used are $h = 15$ and $l = 5$. When t is chosen smaller the 2 models start to overlap.

When t/l is small, meaning the structure consists of long thin beams, the behavior is dominated by the flexure mechanism. As t/l increases, shear and strain start to contribute to the behavior of the Re-entrant Honeycomb. This effect is illustrated in Figure 4-7, where the force transmission is plotted for different values of t while keeping l constant.

4-1-2 Expectations

The calculated effective properties (ν_{xy}, ν_{yx}, E_x and E_y) from Gibsons model, from now on referred to as the Flexure Model, and from Masters and Evans model, from now on referred to as the Complete Model, are used to calculate the force transmission as defined in Equation 4-2.

Considering the Flexure model, influential parameters are the angle θ and the the relation h/l. The constraint for θ is $0 < \theta < \frac{1}{2}\pi$. The stiffness has to be positive, this leads to the constraint for h/l as $h/l + \sin\theta > 0$ has to hold. The same constraints hold for the Complete model.

The theoretical effect of parameters h/l and θ on the force transmission for both models is plotted in Figure 4-8. For higher θ the force transmission increases. For higher h/l ratios the force transmission stays constant or decreases depending on the model.

From the theoretical analysis some conclusions are drawn. Firstly, the parameter that has the most influence on the force transmission is θ. Secondly, the shearing and hinging effects that

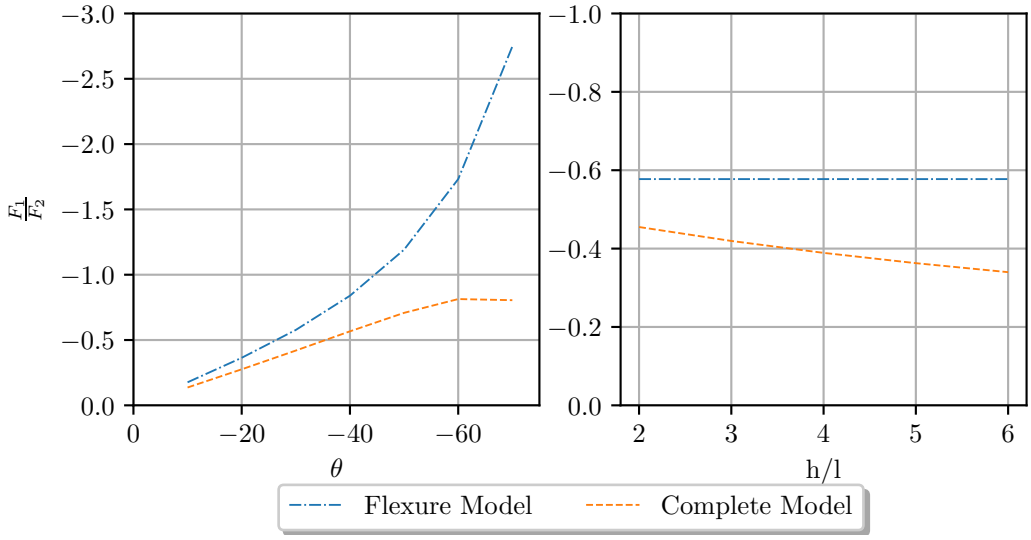

Figure 4-8: The absolute force transmission as described in Equation 4-2, plotted for θ and h/l. Values for used are $t = 1$ mm, $\theta = -30°$ and $h/l = 15/5$. These values correspond to the fabricated structures.

start to contribute to the structure behavior for larger (t/l) have a negative effect on the force transmission. In order to get a high force transmission a structure with thin long beams, i.e. a small t/l and flexure dominated effective properties, is preferred. Thirdly, although the ratio h/l is an important parameter for changing the effective Poisson ratio and Young Modulus, it is expected to have little effect on the force transmission. Finally, from considering both the Flexure Model and the Complete Model uniform down scaling is not expected to have influence on the force transmission behavior. In reality there is a certain limit to the down scaling due to challenges in fabrication of thin beamed structures.

4-2 Methodology for Measuring Force Transmission

This section describes the experimental validation of the described model for force transmission in auxetic structures. First, the fabricated structures are discussed. Next, the experimental setup and the measurement procedure is explained. The results from the experiments are compared to the expectations from theory.

4-2-1 Samples

For this experiment, 9 structures are fabricated from FLEX45 material from RS-Pro with a Prusa MK3. The FLEX material has a Young Modulus of $E_s = 95$ MPa. The choice for the more flexible filament is based on the measurement range of the available force sensors. The geometric parameters and calculated effective properties of the 9 fabricated structures can be found in Table 4-1. The samples B.1 to B.4 have varied values for h/l. For the samples B.5 to B.9 θ is varied. All the samples B.1 to B.9 consist of 3×8 unit-cells. On the left and right boundary of the auxetic structure two beams were added for connection purposes. Images of the samples are shown in Figure 4-9 and 4-10. For all samples $t/l = 0.2$. Considering Figure 4-7, the shearing and straining mechanisms are expected to significantly contribute to the force transmission. The samples set B is designed with the goal to validate the model for force transmission. In section 4-4, when the model has been validated, structures with optimal design parameters for force transmission are considered.

Sample	h [mm]	l [mm]	θ [deg]	t [mm]	ν_{21}	E_1 [MPa]	E_2 [MPa]
B.1	10	5	-30	1	-0.86	1.4	1.5
B.2	15	5	-30	1	-0.52	2.1	0.9
B.3	20	5	-30	1	-0.37	2.8	0.7
B.4	25	5	-30	1	-0.29	3.3	0.5
B.5	15	5	-10	1	-0.85	1.8	3.8
B.6	15	5	-20	1	-0.72	1.9	1.7
B.7	15	5	-40	1	-0.35	2.7	0.5
B.8	15	5	-50	1	-0.23	3.8	0.4
B.9	15	5	-60	1	-0.13	6.1	0.2

Table 4-1: The data for the samples used in experiment. Samples $B.1 - B.4$ are designed to have different h/l ratios. The set of samples $B.5 - B.9$ is designed by only varying θ.The values for ν_{12}, E_1 and E_2 are calculated using the complete model [17].

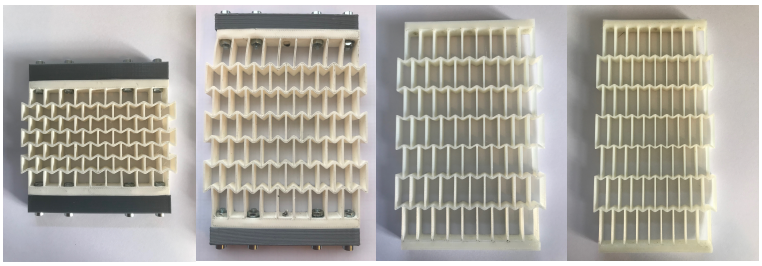

Figure 4-9: Samples B.1 to B.4. The dimensions are documented in Table 4-1

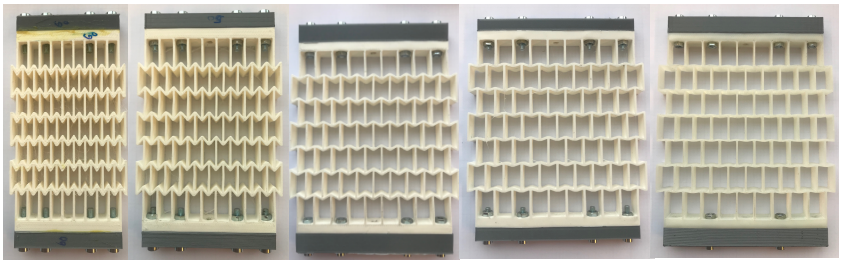

Figure 4-10: Samples B.5 to B.9. The dimensions are documented in Table 4-1

4-2-2 Experimental Setup

In Figure 4-11 and 4-12 a schematic of the experiment and the real experiment is shown respectively. The auxetic structure is constrained in x on the right side. The bottom boundary has a roll constraint and is fixed in y, in reality this is a contact surface between the auxetic structure and an aluminum bar which leads to friction in the x direction.

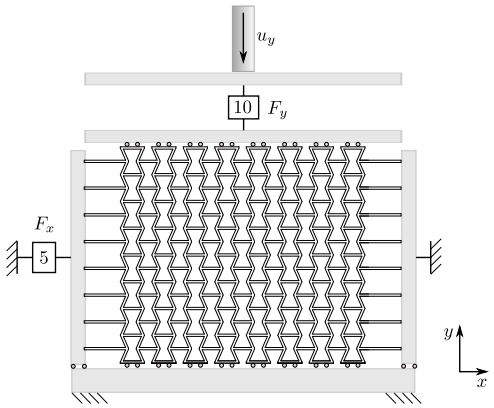

Figure 4-11: Schematic of experiment used to determine the force transmission of auxetic structures.

The left boundary is attached to a Futek LSB200 loadcell with a maximum load capacity of 22.5 N. This sensor is calibrated to a measurement range of $0 - 20$ N for 10 V. On the top boundary a displacement in y is applied, while the force is measured with a Futek LSB200 load cell with a maximum load capacity of 45 N. This sensor is calibrated for the range of

$0 - 40$ N.

The read-out device, a *National Instruments NI USB-6008*, has resolution of 12 bit, this results in a very accurate force resolution for both sensors of higher than 0.0001 N.

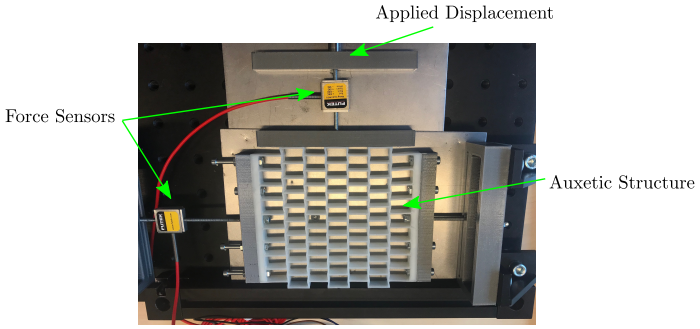

Figure 4-12: Image of the experiment with sample $B.6$.

4-2-3 Measurement Procedure

The sample attached to the force sensors and the fixed boundaries of the setup. A displacement is applied using the micrometer on the top boundary until it contacts the sample. At this point, the load-cells are calibrated to zero. A displacement is applied in steps of 0.25 mm, taking measurements of the Forces on each step. The total displacement applied varies per sample as their Young Moduli vary. A maximum input force of around 30 N is kept as a guideline for this. For every structure this process was repeated five times. The structure surrounding the sample is designed to hold samples of different sizes while keeping the sensors and the applied displacement exactly in the middle of the structure. This makes it easier to swap structures between experiments. This procedure is repeated for all Samples $B.1$ to $B.9$.

4-3 Results

First, the samples B.1 to B.4 with varying h/l are investigated. In Figure 4-13 the retrieved forces F_1 and F_2 are plotted. The force transmission for a sample is determined by taking the gradient of F_1 and F_2. As h/l increases the force transmission decreases. An overview of the experimentally retrieved force transmission for all samples is plotted in Figure 4-15 next to the predictions from theory.

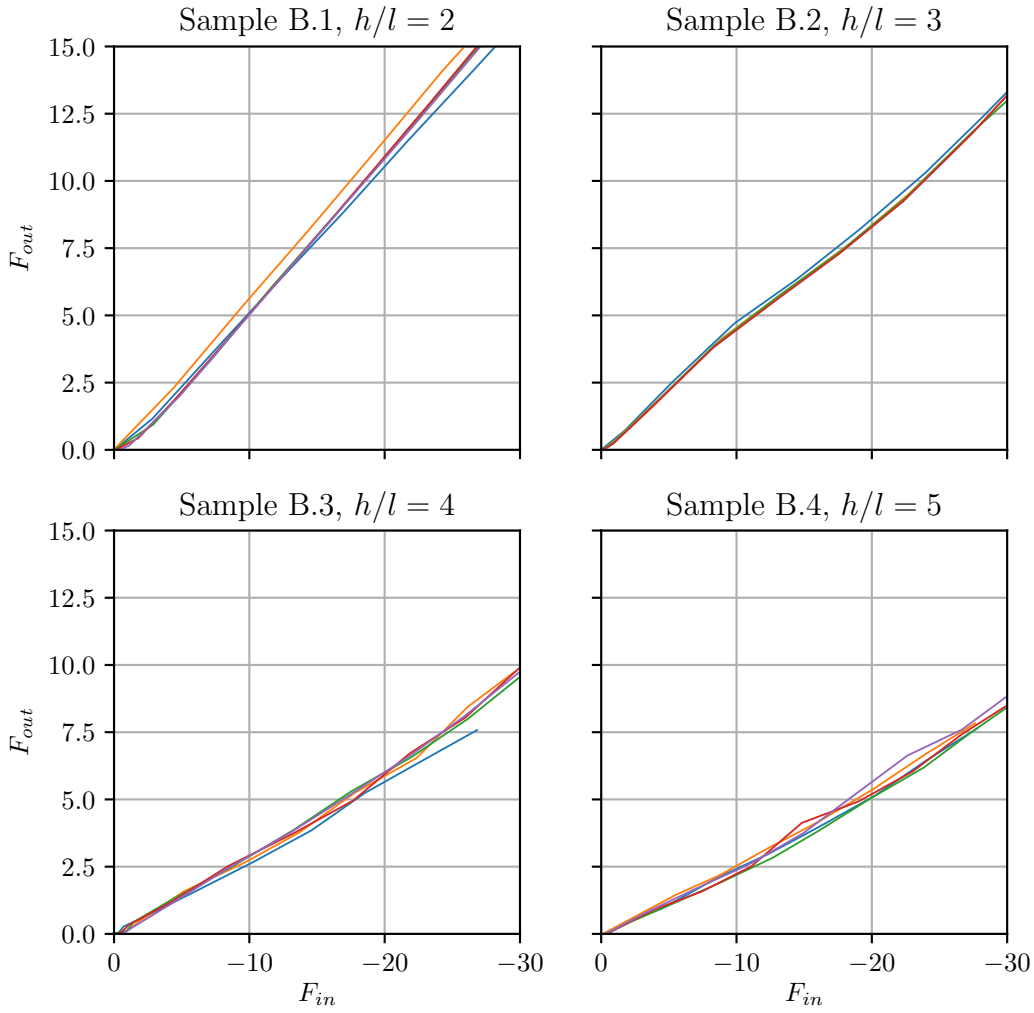

Figure 4-13: F_{in} versus F_{out} for sample $B.1 - B.4$. For every sample the measurement has been repeated 5 times.

In Figure 4-14 the results for samples $B.2$ and $B.5 - B.8$ is plotted. Varying θ has a significant and a non linear effect on the force transmission.

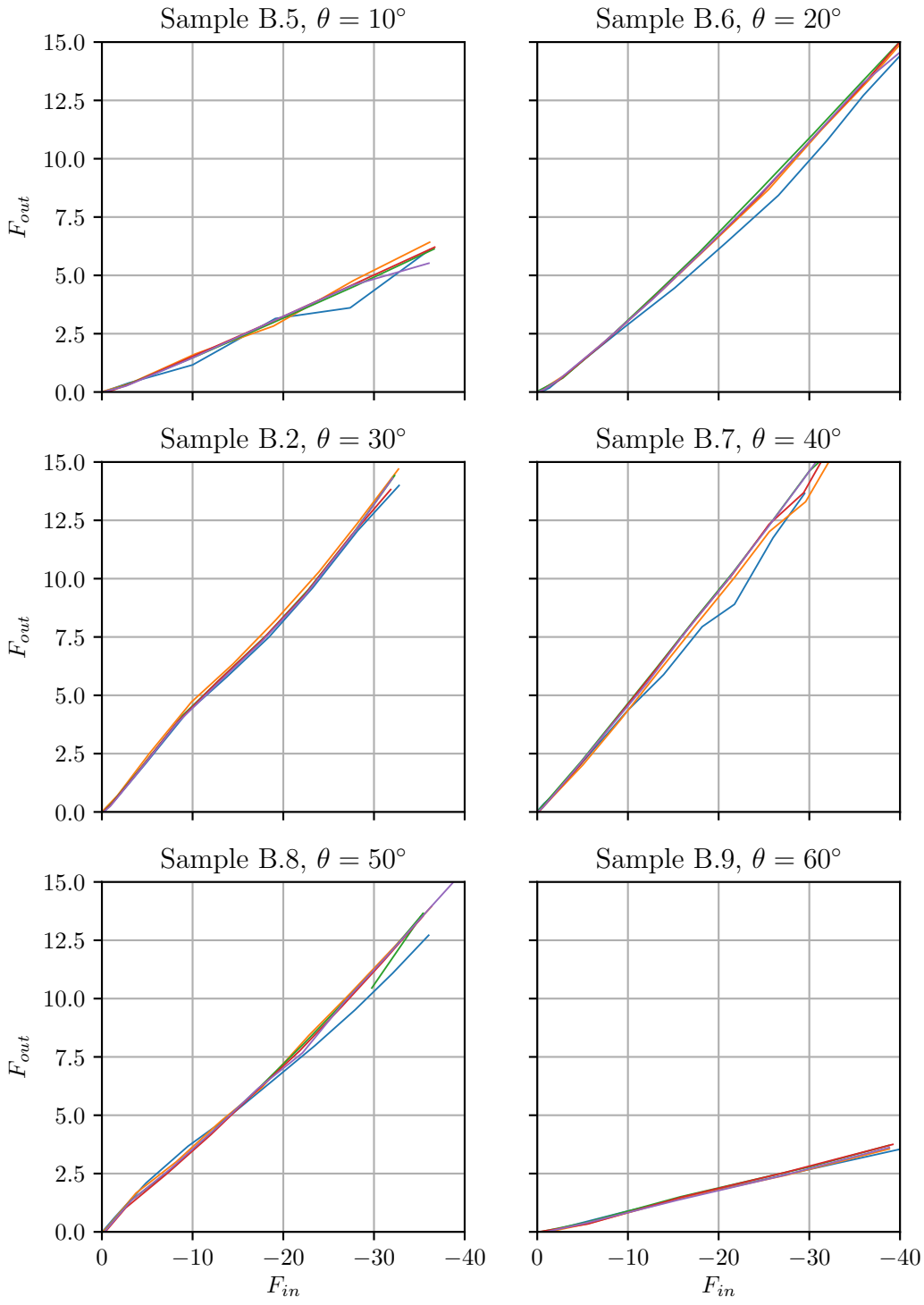

Figure 4-14: F_{in} versus F_{out} for samples $B.2$ and $B.5 - B.8$. For every sample the measurement has been repeated 5 times.

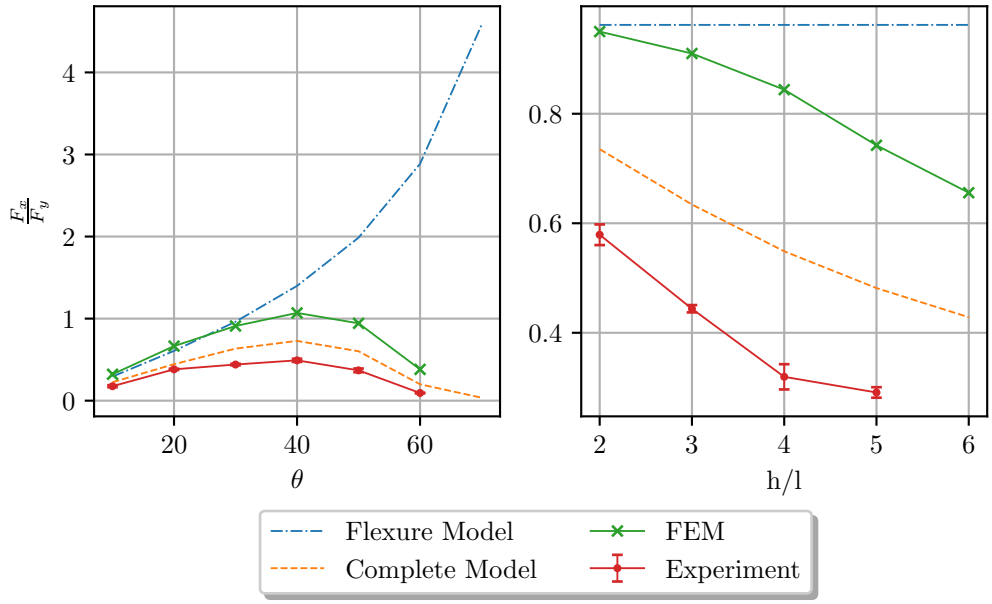

Figure 4-15: Comparison of absolute force transmission F_x/F_y from theory, experiments and Comsol model. The force transmission is plotted versus the absolute angle $\mid \theta \mid$ and h/l. The value of force transmission is the average of all 5 runs, at a strain of 1%.

The average of the gradients over all repetitions is plotted in Figure 4-15. The errorbars indicate the standard deviation of the repetitions. It was noticed that the geometric description of the re-entrant honeycomb is dependent on the beam thickness t, to take this into account the description was modified. This modification is explained in subsection 4-3-1. The theory that is plotted in Figure 4-15, uses this modification. Besides the theory, a FEM model of the complete structure is made to verify the experimental results. The details for this simulation are documented in Appendix E.

4-3-1 Addition to the Geometric Description of Re-entrant Honeycombs

The geometric description of a Re-entrant Honeycomb is defined as a structure of ligaments without considering the beam thickness t by Masters and Evans [17]. It was found that for high angles of θ, the length of the bending part of a ligament is influenced by the beam thickness t. This is illustrated by Figure 4-16, which shows one corner of the structure. This effect is present at both sides of a beam.

To compensate for this, the effective lengths h_e and l_e are defined in Equation 4-9, α is defined in Figure 4-16.

$$\begin{aligned} l_e &= l - 2l_t = l - \frac{t}{\tan\alpha} \\ h_e &= h - 2h_t = h - \frac{t}{\tan\alpha} \end{aligned} \tag{4-9}$$

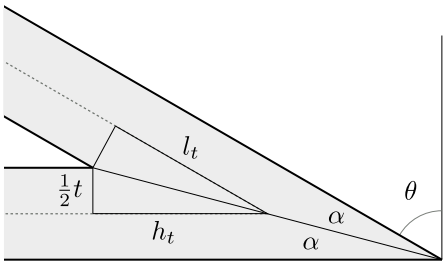

Figure 4-16: Schematic that illustrated the effect of beam thickness t on the geometry of the re-entrant honeycomb. When θ increases the beam thickness starts to significantly decrease the length of the beams.

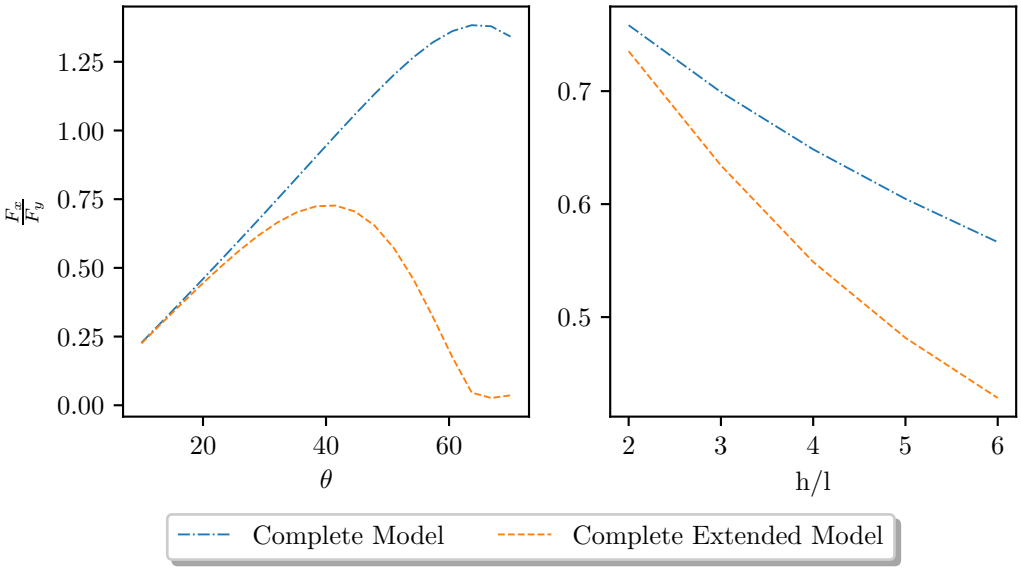

Figure 4-17: Plot of the extended model using effective lengths l_e and h_e versus the Complete model.

Using the effective lengths instead of l and h results in a higher contribution of the shearing and straining mechanisms. This effect is shown in Figure 4-17.

4-4 Design for Maximum Force Transmission

Now that the model for force transmission is verified, the next step is to design for high force transmission. The curve of the flexure model in Figure 4-15, indicates that is possible to achieve very high force transmission when there is no contribution of the shear and strain mechanisms. As θ is increased F_x/F_y increases exponentially. In reality there is always contribution of the shear and strain mechanisms, but it can be minimized by designing for small t/l ratios.

4-4-1 Simulation

To verify this expectation, and to see if the re-entrant structure can be pushed to extremes a simulation is performed. For the simulation, 2D geometries of one unit-cell with a small t/l ratio for increasing θ are constructed. An example of the geometry and mesh is used is in Figure 4-18, the details for the used geometries can be found in section E-2. A quadrangular mesh with element size $h_{max} = 0.4$ mm was used.

On the top of the unit-cell a prescribed vertical displacement of $u_y = -1$ mm is applied. The bottom boundary is constrained in y and the sides of the structure are constrained in x direction. The reaction forces on the side boundary and the top boundary are used to calculate the force transmission.

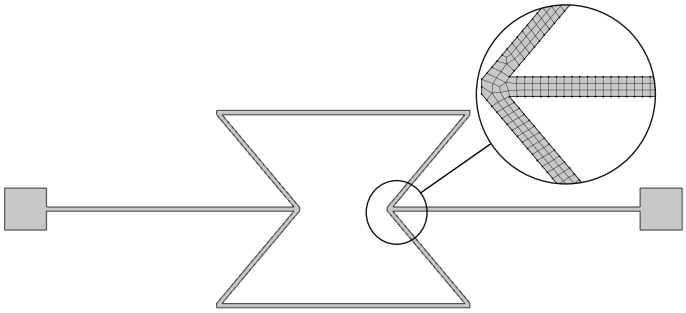

Figure 4-18: Geometry and mesh used for Comsol simulation for re-entrant structures with extreme design parameters. In this image the structure with $\theta = 40°$ is seen.

The results are plotted against the Complete modified model in Figure 4-20. For $\theta = \{40°, ..., 78°\}$, a beam thickness $t = 1$ mm was used. It can be seen that the curve starts to deviate from flexure theory at higher angles. This is due to the effective length of l getting smaller as the hinge gets more bulky and the behavior becomes less flexure dominated. A way to reduce this effect is to further decrease beam thickness to $t = 0.5$ mm. By doing this for $\theta = \{80°, ..., 84°\}$, a high force transmission is achievable.

4-4-2 Experimental Verification

To verify this finding, Sample C.1 and C.2 with high angles of θ were fabricated with the geometric parameters listed in Table 4-2. The samples are shown in Figure B-4. The force transmission for these samples was measured using the experimental setup described in subsection 4-2-2.

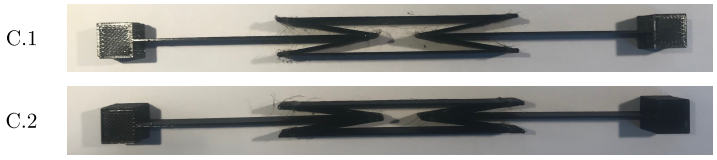

Figure 4-19: Samples C.1 and C.2

Sample	θ [deg]	h [mm]	l [mm]	t [mm]	v_{yx}	E_x	E_y
C.1	-80	70	30	0.5	-0.022	2.09 MPa	1137 Pa
C.2	-82	70	30	0.5	-0.015	3.94 MPa	905 Pa

Table 4-2: Samples C.1 and C.2 and their geometric properties and theoretical effective properties v_{yx}, E_x and E_y. The structure consists out of one unit cell. The material used is PET ($E_s = 1.85$ GPa)

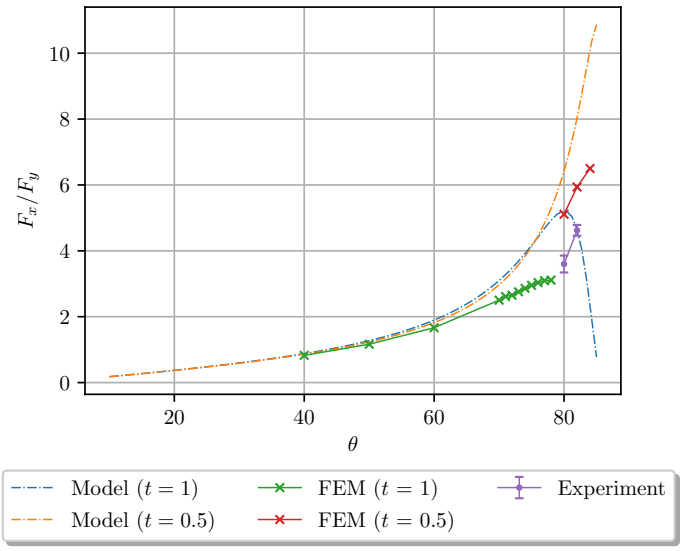

Figure 4-20: The results of the simulation for re-entrant structures with extreme design parameters.

4-5 Discussion of Results

For varying h/l, the experimental results as well as the theoretical and numerical results show a decreasing trend when h/l increases. The values that are measured are consistantly lower than theory and simulations. In theory and simulations, it is assumed that there is no strain in x direction. In the experiment there is some compliance, which explains the lower measured force transmission. Another reason is that the top and bottom boundaries affect the behavior of the structure. In the model and simulation these boundaries are assumed to only be constrained in y, but in reality there is also a friction force in x that increases when the structure is loaded.

In Figure 4-15 a peak in force transmission is noticed at $\theta = 40°$. This peak shifts to the right when t/l is chosen smaller and the shearing and straining effect lose their contribution to the effective material properties. This is seen in Figure 4-20. Simulation of a second iteration of re-entrant structures of only one unit-cell with high angles of θ, indicates that high force transmission in an auxetic metamaterial is possible. The results from this simulation are in agreement with the expectations, that force transmission increases exponentially for increasing θ. Two of the designs, with $\theta = 80°$ and $\theta = 82°$, are fabricated and the force transmission is measured in an experiment. The maximum force transmission that was measured is 4.6 for $\theta = 82°$. This result is lower than the expected values from theory and the simulation but follows the same trend. This difference is probably caused by the extra compliance, introduced in the experimental setup.

4-6 Conclusion

From the results of this chapter, potentially well performing structural designs are found. The Re-entrant structure type proved to be a suitable auxetic structure type for pressure to strain conversion. Defining the relation between force transmission and effective properties, resulted in this expectation. The expectation was verified by measuring the force transmission in an experiment.

It is found that when Re-entrant Honeycombs are designed with high angles of θ, the effective lengths of the bending beams change. By introducing effective lengths l_e and h_e and using them in the model of Masters and Evans, results in a better estimation of effective properties.

Chapter 5

Conclusive Chapter

Conclusion

In this chapter a conclusive answer is described, to the question how an auxetic metamaterial can be used as an intermediate for converting pressure from the fluid domain to strain in the mechanical domain.

Auxetic metamaterials have the potential to offer strain enhancement in a solid in small form factor. For the created strain per Pascal (nanostrain Pa^{-1}) the auxetic metamaterial approach achieves similar strains as existing approaches. Additionally, the straining behavior created by auxetic metamaterials is expected to be linear.

Experimental evaluation of the Poisson ratio of 2D auxetic structures shows that the boundary effects cause the unit-cells close to the boundaries to behave completely different from what the structure is designed for. It is found that to accurately verify the effective Poisson ratio for which an auxetic structure is designed, the method using a rectangular plane is the most effective. The *Anti* and *Meta* Tetra Chiral structures considered in this research consist of 10×12 and 10×14 unit-cells respectively. For both structures, the effect of the fixed boundary was found to be insignificant at a distance of $n = 4$ unit cells. The effect of the free boundary dissipated at a distance $m = 3$ unit cells from the free boundary. This is the region in the auxetic material where the structure behaves as if it is unconstrained and there is no significant effect of the fixed or free boundaries on the behavior of the structure.

The Re-entrant Honeycomb auxetic structure type provides the most potential for pressure to strain conversion when the auxetic metamaterial is not directly fixed to the fiber but to stiff end plates. This links the potential for pressure to strain conversion to the concept of force transmission.

Re-entrant Honeycombs can be designed for a large range of an-isotropic effective properties which is beneficial for force transmission. For increasing angles of θ, which is a key design

parameter in the re-entrant structure, an exponential increase of the force transmission was expected. Experiments measuring the force input and output while applying a deformation to the structure, confirm this expectation.

In modeling the force transmission for Re-entrant Honeycombs by using the model described by Master and Evans [17], it is important to use the effective beam lengths, l_e and h_e, for larger θ. This effectively causes a higher contribution of the shearing and straining mechanisms to the flexure dominated equations. This expanded model matches the results from the experiment.

Recommendations

From the investigation of auxetic metamaterials for pressure from the fluid domain to strain in a solid domain, lead to looking at auxetic structures from a force transmission perspective. It was found that Re-entrant Honeycombs with extreme geometries are potentially well-performing in pressure to strain conversion.

Single Unit Cell

Using this insight a quick study has been performed on a concept sensor design using axial and radial pressure. In Figure 5-1 a simulation of this concept is shown. A geometry with the shape of an auxetic unit-cell is attached to the fiber, converting radial pressure into axial strain. The rigid disks on both sides of the sensor are used to convert axial pressure into axial strain.

This example shows that in the area indicated by the circle there is a maximum axial strain of 1.36 nanostrain Pa^{-1}. This is a simulation of a 2D case, with diameter of the fiber $d_f = 50$ μm and maximum diameter $d_{max} = 330$ μm. The estimation of a strain of 1.36 nanostrain Pa^{-1} that follows from this estimation, is well above the required sensitivity of 0.1 nanostrain Pa^{-1} needed to measure blood pressure differences caused by obstructions in arteries.

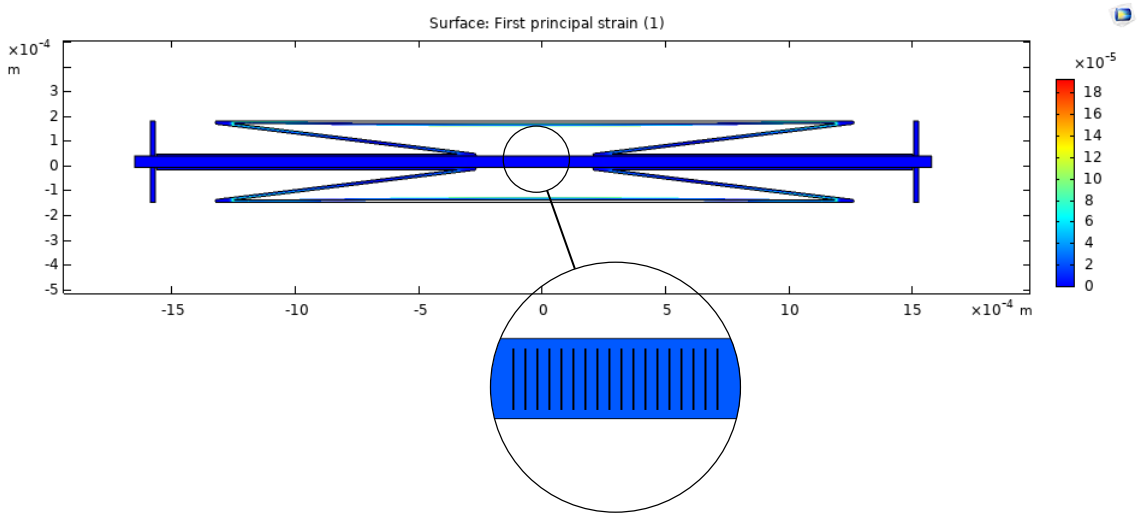

Figure 5-1: A quick study to demonstrate the non-uniform axial strain distribution in the fiber, when the auxetic material is directly fixed to the fiber. An axial strain of 1.36 nanostrain Pa^{-1} was found.

Using a radial pressure to axial strain converter, as well as the axial pressure is a promising field to investigate further. In the example of Figure 5-1, this pressure converter was shaped as a Re-entrant Honeycomb unit-cell. It is recommended that other geometries are investigated, improving the strength of the structure. Another aspect to consider is the fabrication of these kind of concepts. It raises questions as: How can the structure be attached to a fiber for best

pressure to strain conversion and is it possible to create a functioning thin beamed structure considering the maximum dimensions of 330 μm.

Multiple Unit Cells

When the equation for force transmission(Equation 4-2) is considered, it is noted that a high L_y/L_x ratio is beneficial the force transmission. For Re-entrant honeycomb unit-cells, a high force transmission is achieved for high L_x and low L_y. To achieve higher force transmission the unit-cells can be stacked vertically. In Figure 5-2 this concept is shown. This example achieves a force transmission of over 34. The unit-cell that is used in this example is *Sample C.1.* Scaling down unit-cells, that have high force transmission, and creating an auxetic structure with large L_y and small L_x theoretically improves the force transmission significantly. It has to be investigated what the limits are in scaling down these structures in terms of the robustness of the thin beams. There will be a middle ground between the concept in Figure 5-1, that consists of one big unit-cell with relatively thick beams, and the concept in Figure 5-2 that consists of multiple smaller and less robust unit-cells.

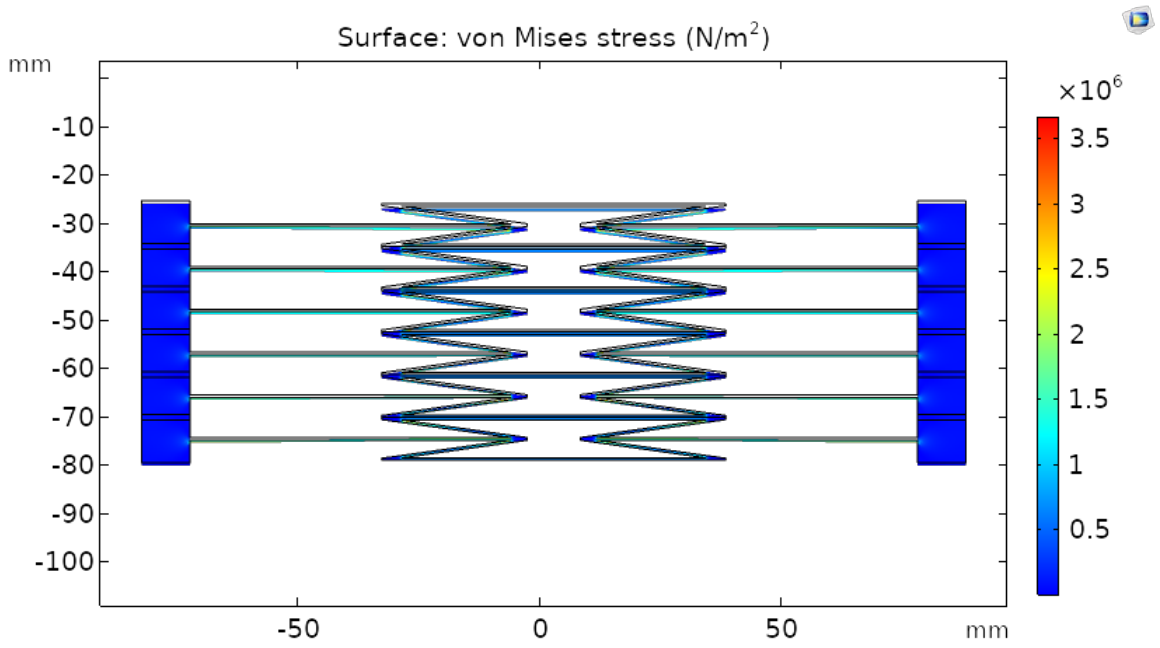

Figure 5-2: A quick study of stacked unit-cells to increase force transmission

Appendix A

Properties of Auxetic Structures

A-1 Tetra Chiral Structures

A Tetra Chiral unit-cell consists of a rigid ring and 4 ligaments. Through ordering the unit-cells in different ways, the structures shown in Figure A-1 are created. In this section the theoretical analyses of these 2 structure types are discussed.

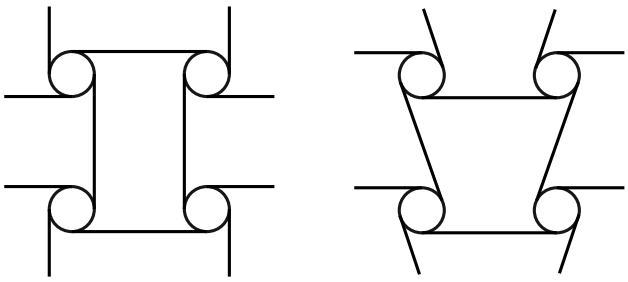

(a) Anti Tetra Chiral structure type. **(b)** Meta Tetra Chiral structure type.

Figure A-1: Different possibilities for Tetra Chiral structures

A-1-1 Tetra Chiral

A-1-2 Anti Tetra Chiral

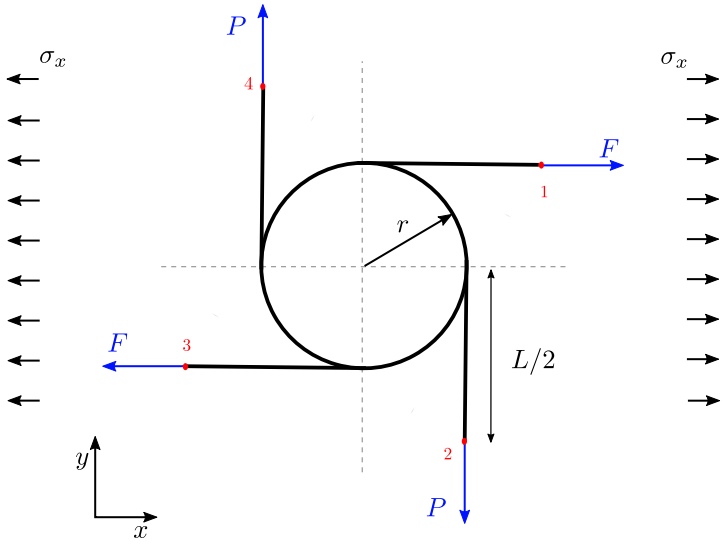

Figure A-2: Free Body Diagram of an Anti Tetra Chiral unit-cell.

The structure is built by mirroring the unit cells over the boundaries of the unit cell. Again following the method of Mousanezhad et al. [19] eqs. (A-1) and (A-2) are obtained. When radius r is significantly larger than beam thickness t, the effective Poisson ratio is simplified as -1. Other models derive the Poisson ratio from the rotation of a rigid ring this predicts a Poisson ratio of -1 [20].

$$E_x/E_s = \frac{t/L}{1 + 6(r/L)^2/(t/L)^2} \tag{A-1}$$

$$v_{xy} = \frac{-6(r/L)^2}{6(r/L)^2 + (t/L)^2} \tag{A-2}$$

A-1-3 Meta Tetra Chiral

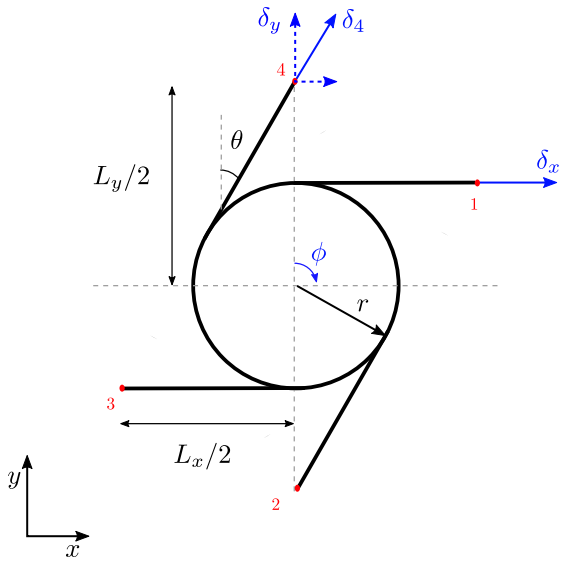

Figure A-3: A schematic of the Meta Tetra Chiral structure, to derive the Poisson ratio v_{xy}.

This type of structure is a combination, also called *meta-chiral* [21], of the normal and Anti Chiral structure, normal in y direction and Anti Chiral in x direction. A schematic of this structure and unit cell is shown in Figure A-3. Because this structure is both Chiral and Anti Chiral the deformation mechanism consists of a full-wave and a half-wave beam deformation. Using the schematic of a unit-cell, shown in Figure A-3, the Poisson ratio is derived, by using the method from Li et al. [16].

When the structure deforms the rigid ring rotates with angle ϕ, under the assumptions that displacements are infinitesimally small, the deformation in x of the unit-cell is the radius times rotation and is thus defined as,

$$\delta_x = (r - 0.5t)\phi \tag{A-3}$$

The deformation along the ligament direction, is defined similarly as,

$$\delta_4 = (r - 0.5t)\phi \tag{A-4}$$

The y component of δ_4 is defined as,

$$\delta_y = \delta_4 \cos\theta \tag{A-5}$$

The strain in x and y are defined as,

$$\epsilon_i = \frac{\delta_i}{L_i/2} \tag{A-6}$$

Where L_i is the length of the unit-cell in the direction of the deformation. This leads to the definition of the Poisson ratio as,

$$\nu_{yx} = -\frac{\epsilon_x}{\epsilon_y} = -\cos\theta \frac{L_y}{L_x} \tag{A-7}$$

It is concluded that there is a mistake in the derivation of the strain in the work of Li et al.[16]. When the correct formula is used, the data from the experiment and numerical model match the expectations from theory.

For calculating the effective properties the model presented by Li et al. [16] is followed. Using the relation between the strain and strain energy(U_i) defined as:

$$\frac{1}{2} E_i \epsilon_i^2 = \sum_{n=1}^{4} \frac{1}{V} U_i \tag{A-8}$$

With the Volume defined as $V = 4L_x L_y h$.

Strain Energy for the Chiral ligaments is defined as,

$$U_{chiral} = \frac{E_s h t^3 \phi^2}{2L_{ey}} \tag{A-9}$$

and is based on a full-wave deformation.

Due to the thickness of the beam, a part of the beam is not bending, as it is coinciding with the rigid ring. The effective lengths of the beams are calculated. Where the effective length in y, L_{ey} is defined as,

$$L_{ey} = \sqrt{L_y^2 - (2r - t)^2} - 2\sqrt{2rt - t^2} \tag{A-10}$$

For the Anti Chiral ligaments the strain energy is,

$$U_{antichiral} = \frac{E_s h t^3 \phi^2}{6L_{ex}} \tag{A-11}$$

Where the effective ligament length in x, L_{ex}, is defined as,

$$L_{ex} = L_x - 2\sqrt{2rt - t^2} \tag{A-12}$$

Combining Equation A-8 A-10 and A-11 , Equation A-13 and A-14 for effective Young Modulus are obtained.

$$E_x = \frac{2\left(\frac{E_s t^3}{2L_{ey}} + \frac{E_s t^3}{6L_{ex}}\right)\left(\frac{L_x}{2r-t}\right)^2}{L_x L_y} \tag{A-13}$$

$$E_y = \frac{2\left(\frac{E_s t^3}{2L_{ey}} + \frac{E_s t^3}{6L_{ex}}\right)\left(\frac{L_y}{(2r-t)\cos(\theta)}\right)^2}{L_x L_y} \tag{A-14}$$

A-2 Re-Entrant Honeycomb

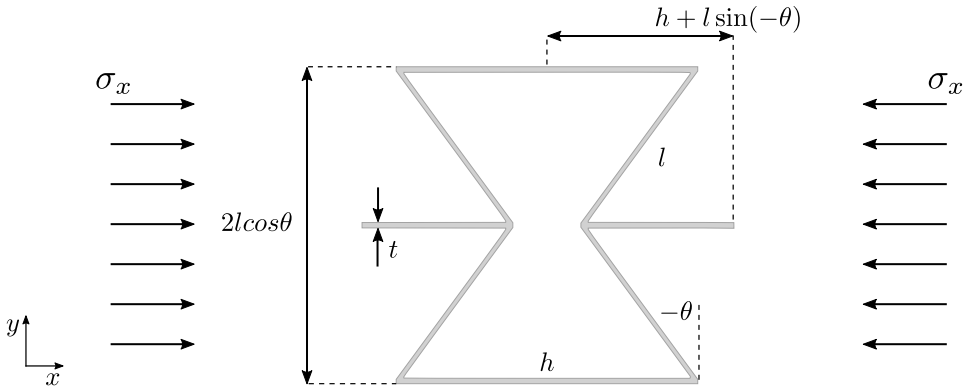

Figure A-4: Schematics of Bowtie

Gibson et al. describe the behavior of a Re-entrant Honeycomb structure, also referred to as a Bow-tie structure[18]. In Figure A-4 a schematic is seen of this structure. There are two types of models. The simple version of the model assumes flexure dominated behavior and only considers the deformation due to flexure of the ribs. This modelis expanded with hinging and straining of the ribs [17].

Flexure Model

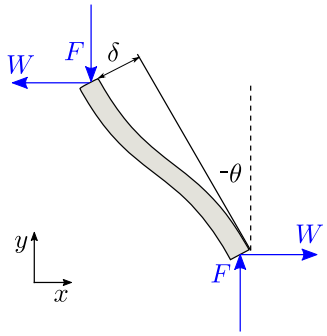

Figure A-5: Bending Beam of length l due to the far field stress σ_x.

The behavior of the re-entrant honeycomb is derived by analysis of the beam in Figure A-5. The geometric parameters used in this derivation are indicated in Figure A-4 The displacement δ follows from standard beam theory as,

$$\delta = \frac{Ml^2}{12E_sI}, \tag{A-15}$$

Where $M = \frac{1}{2}Wl\cos\theta$. Using that force W is caused by the far field stress σ_x, the strain in x can be written as Equation A-16

$$\epsilon_x = \frac{\delta\cos\theta}{h + l\sin\theta} = \frac{\sigma_x bl^4\cos^3\theta}{12E_sI(h + l\sin\theta)} \tag{A-16}$$

From the relation $E_x = \sigma_x/\epsilon_x$, the effective Young Modulus in x direction is obtained as Equation A-17.

$$E_x = E_s \left(\frac{t}{l}\right)^3 \frac{h/l + sin\theta}{\cos^3\theta} \tag{A-17}$$

Masters and Evans [17] define the flexure force constant K_f as in Equation A-18, with b as the out of plane depth.

$$K_f = \frac{E_s b t^3}{l^3} \tag{A-18}$$

Combining Equation A-17 and A-18 results in the Effective Young Modulus in x direction in Equation A-19

$$E_x = K_f \frac{h/l + \sin\theta}{\cos^3\theta b} \tag{A-19}$$

In a similar way the effective Young Modulus in y is derived, resulting in Equation A-20.

$$E_y = K_f \frac{\cos\theta}{\sin^2\theta(h/l + \sin\theta)b} \tag{A-20}$$

The strain in y, due to the displacement δ is defined in Equation A-21.

$$\epsilon_y = \frac{\delta \sin\theta}{l \sin\theta} \tag{A-21}$$

Combining Equation A-21 and A-16, the Poisson ratio is retrieved as Equation A-22.

$$\nu_{yx} = -\frac{\epsilon_x}{\epsilon_y} = \frac{\cos^2\theta}{(h/l + \sin\theta)\sin\theta} \tag{A-22}$$

Complete Model

To include hinging and straining effects, Masters and Evans define force constants K_s for strain and K_h for hinging as in Equation A-23 [17].

$$\begin{aligned} K_s &= \frac{E_s b t}{l} \\ K_h &= \frac{G_s b t}{l} \end{aligned} \tag{A-23}$$

Combining the effect of flexure, hinging and strain into one general model Masters and Evans define the effective properties of a Re-entrant Honeycomb as in Equation A-24.

$$
\begin{aligned}
E_x &= \frac{1}{\frac{b\cos\theta}{h/l+\sin\theta}\left[\frac{\cos^2\theta}{K_f}+\frac{\cos^2\theta}{K_h}+\frac{2h/l+\sin^2\theta}{K_s}\right]} \\
E_y &= \frac{1}{b(h/l+\sin\theta)\left[\frac{\sin^2\theta}{K_f\cos\theta}+\frac{\sin^2\theta}{K_h\cos\theta}+\frac{\cos\theta}{K_s}\right]} \\
\nu_{xy} &= -\sin\theta(h/l+\sin\theta)\left[\frac{-\frac{1}{K_f}-\frac{1}{K_h}+\frac{1}{K_s}}{\left[\frac{\cos\theta^2}{K_f}+\frac{\cos^2\theta}{K_h}+\frac{2h/l+\sin^2\theta}{K_s}\right]}\right] \\
\nu_{yx} &= \frac{-\sin\theta\cos\theta\left[\frac{1}{K_f}+\frac{1}{K_h}-\frac{1}{K_s}\right]}{(h/l+\sin\theta)\left[\frac{\sin^2\theta}{K_f\cos\theta}+\frac{\sin^2\theta}{K_h\cos\theta}+\frac{\cos\theta}{K_s}\right]}
\end{aligned}
\tag{A-24}
$$

Appendix B

Samples

Samples A.1-2

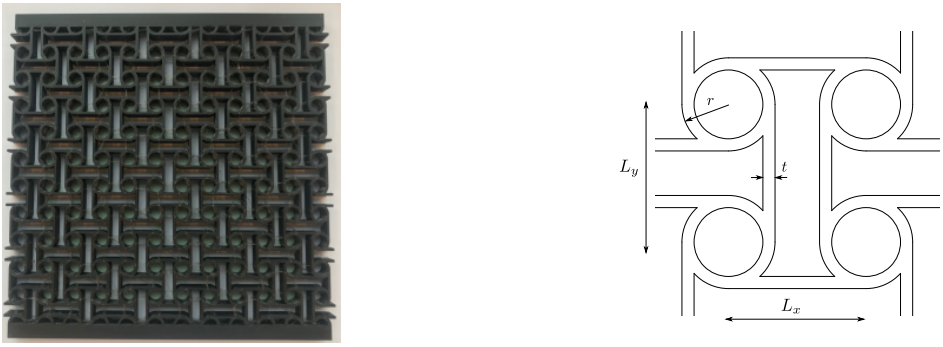

Figure B-1: Sample 1.A -An Anti Tetra Chiral structure, 12×10 unit-cells. Design Parameters are : $L = 25$ mm, $r = 5$ mm and $t = 1.5$ mm

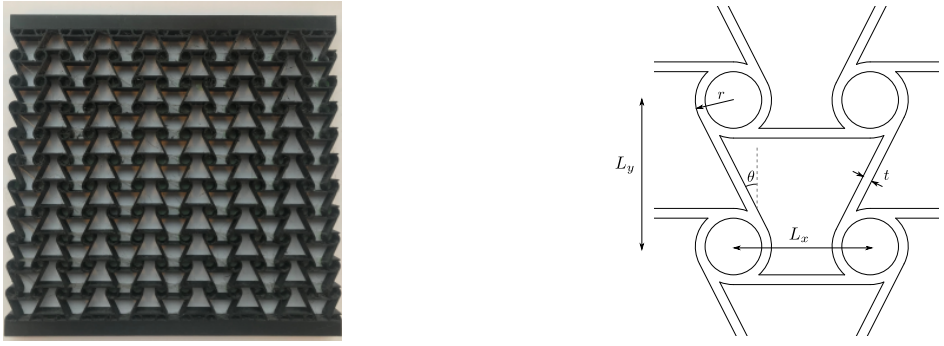

Figure B-2: Sample 1.A - A Meta Tetra Chiral structure, 14×10 unit-cells. Design Parameters are : $L_x = 14$, $L_y = 15$, $r = 4$ and $t = 1$.

Samples B.1-9

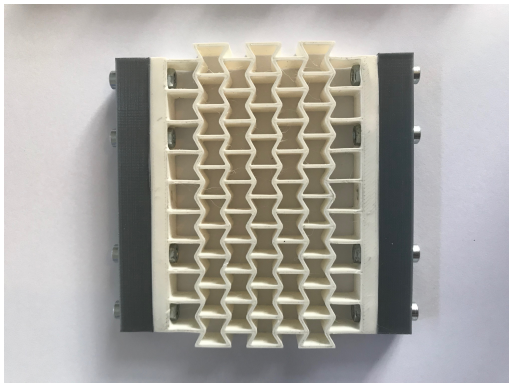

(a) Sample B.1

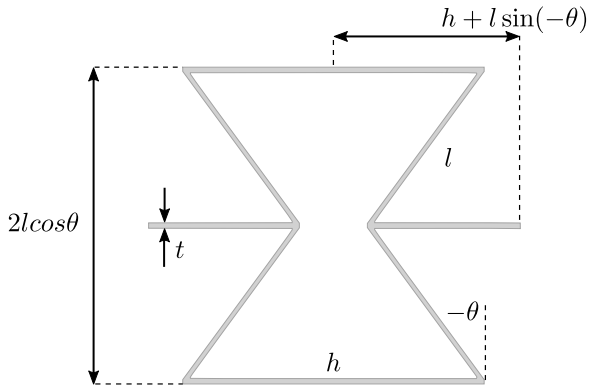

(b) Schematic of a Re-entrant Honeycomb unit cell.

Sample	h [mm]	l [mm]	θ [deg]	t [mm]	ν_{21}	E_1 [MPa]	E_2 [MPa]
B.1	10	5	-30	1	-0.86	1.4	1.5
B.2	15	5	-30	1	-0.52	2.1	0.9
B.3	20	5	-30	1	-0.37	2.8	0.7
B.4	25	5	-30	1	-0.29	3.3	0.5
B.5	15	5	-10	1	-0.85	1.8	3.8
B.6	15	5	-20	1	-0.72	1.9	1.7
B.7	15	5	-40	1	-0.35	2.7	0.5
B.8	15	5	-50	1	-0.23	3.8	0.4
B.9	15	5	-60	1	-0.13	6.1	0.2

Table B-1: The data for the samples used in experiment. Samples $B.1 - B.4$ are designed to have different h/l ratios. The set of samples $B.5 - B.8$ is designed by only varying θ.The values for ν_{12}, E_1 and E_2 are calculated using the expanded model [17].

Samples C.1-2

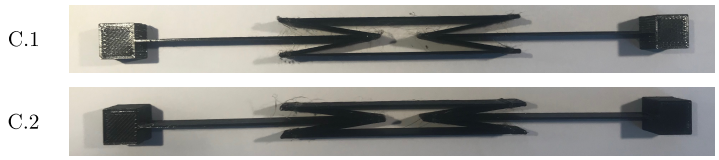

Figure B-4: Samples C.1 and C.2

Sample	θ [deg]	h [mm]	l [mm]	t [mm]	v_{yx}	E_x	E_y
C.1	-80	70	30	0.5	-0.022	2.09 MPa	1137 Pa
C.2	-82	70	30	0.5	-0.015	3.94 MPa	905 Pa

Table B-2: Samples C.1 and C.2 and their geometric properties. The structure consists out of one unit cell. The material used is PET ($E_s = 1.85$ GPa), parameters are defined in Figure B-3b

Appendix C

Fabrication

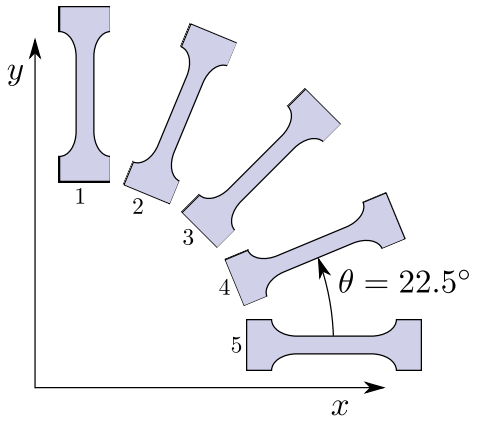

Figure C-1: Printing Directions for determining relation between printing direction and Young Modulus.

Influence of Printing Direction

The printer used is a *Prusa MK2*. The printing material used is "RS PRO-PET-G" 1.75 mm filament. Literature shows that the Young Modulus of a printed material varies with printing direction [22]. To see what the effect of printing direction on Young Modulus, while using the Prusa setup, a tensile test is performed. 5 Dogbones where printed, for different angles as seen in Figure C-1. Important to notice is that the 3D printer first prints the outline of a plane, to later fill it up. The printing direction only influences the pattern of this second part, as when printing the outline it follows the outline direction. Combining this with the fact that the to be printed auxetic structures consist of thin beams, the dogbones dimensions where chosen accordingly(mostly consisting of outline). This research focuses on 2D auxetic structures, this is why only printing angle θ in the $x-y$ plane is varied.

The 'Zwick Roell' tensile/ compression machine was used to perform the tensile test. This machine has a load capacity of 1000 N. The Young modulus of the PET filament, provided by the manufacturer, is E = 2150 MPa and yield strength of σ_Y =50 MPa.[**?**]. The cross sectional area A_c of the dogbone is 25 mm^2. So a 1250 N Load is necessary to reach the yield strength. This is higher than the load capacity of the Zwick Roell machine, meaning that only the first part of the stress-strain curve can be obtained. As we are mainly interested in the Young Modulus of the printed material and the variation of this property with respect to the printing angle, loading in the elastic regime is sufficient. The 5 samples were loaded until 1000 N resulting in the stress-strain curves as displayed in Figure C-2.

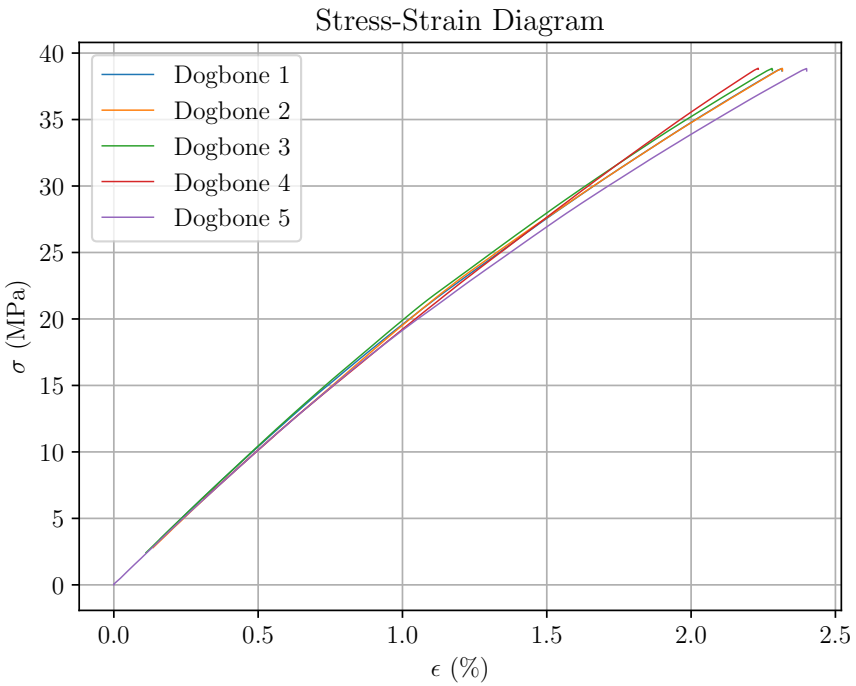

Figure C-2: The stress-strain curve resulting from Tensile test for different printing angles.

The Young Modulus was retrieved from the data using $E = \sigma/(\delta/L0)$. Where L_0 was chosen the distance between the grippers. δ is the displacement and $\sigma = F/A_c$ where A_c is the cross sectional area. From the results in Table C-1, it is seen that the printing direction(under our conditions) has little effect on the behaviour of the material. The mean value is E = 1.85 GPa for 3D printed PET.

Sample	Rotation θ	Young Modulus (MPa)
1	90°	1834
2	67.5°	1842
3	45°	1871
4	22.5°	1822
5	0°	1863

Table C-1: Young Modulus obtained from experiment.

Appendix D

Calculation of Unit-Cell

For the unit-cells that are not surrounded by 4 other unit-cells, a different approach to calculating the displacements is needed. For the unit-cells on the side the 3 surrounding cells are used with lengths L_x and L_y as in Figure D-1a. For the corner nodes the only 2 surrounding nodes are available, this is illustrated in Figure D-1b

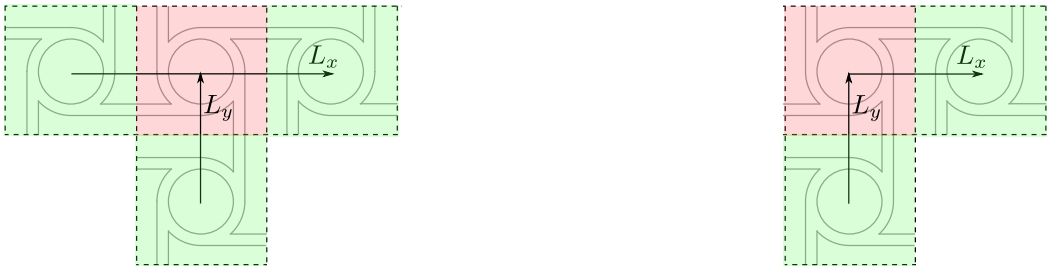

(a) **(b)**

Figure D-1: Methods used to extract Poisson ratio ν_{yx} for unit cells on the boundaries(a) and corners(b).

Appendix E

FEM

E-1 FEM Experiment 2

Finite Elements method used to verify data from the experiment. The complete geometry used in the experiment is modeled consisting of multiple unit cells and the solid boundaries. The problem is analyzed in 2D. The boundary conditions are roll constraints on bottom, left and right. On the top a prescribed displacement is applied of -1 mm compressing the structure. A triangular mesh with extra fine elements is used for 2D, it can be seen in Figure E-1. The reaction forces due to the prescribed displacement are calculated taking a line integration on top (F_2) and left(F_1) bottom. For every geometry (Sample $1-9$) this simulation is done. The results from the simulations are seen in Table E-1.

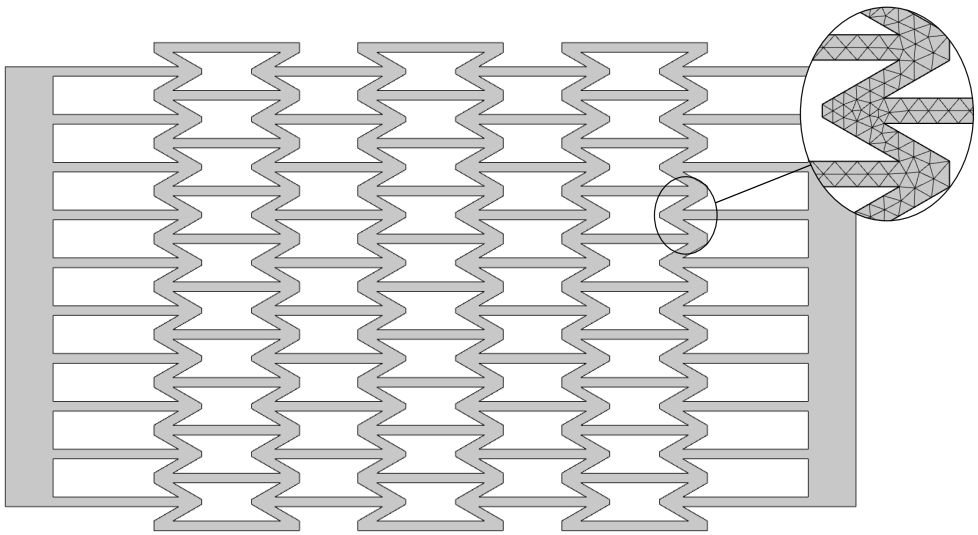

Figure E-1: Triangular mesh used for 2D case

	Linear			Geometric Non Linear		
θ [deg]	F_1 [N/m]	F_2 [N/m]	Ratio	F_1 [N/m]	F_2 [N/m]	Ratio
10	-2154.7	-6281.6	0.34	-2308.6	-6133.4	0.376398083
20	-3243.9	-4556.3	0.71	-3342.2	-4428	0.754787715
30	-3305.2	-3154.3	1.05	-3353.8	-3080.9	1.088578013
40	-2952.8	-2477	1.19	-2987.4	-2433.5	1.227614547
50	-2510.5	-2350.9	1.07	-2544.6	-2311.2	1.100986501
60	-2113.8	-3805.2	0.56	-2158.8	-3693.2	0.584533738

Table E-1: Results from the 2D FEM simulation. The problem was solved for linear and geometric non linear case. Geometric non-linearity is important to consider when displacements are large. Considering the pressure differences are small in the eventual application, the linear results are used.

E-2 FEM Unit Cells

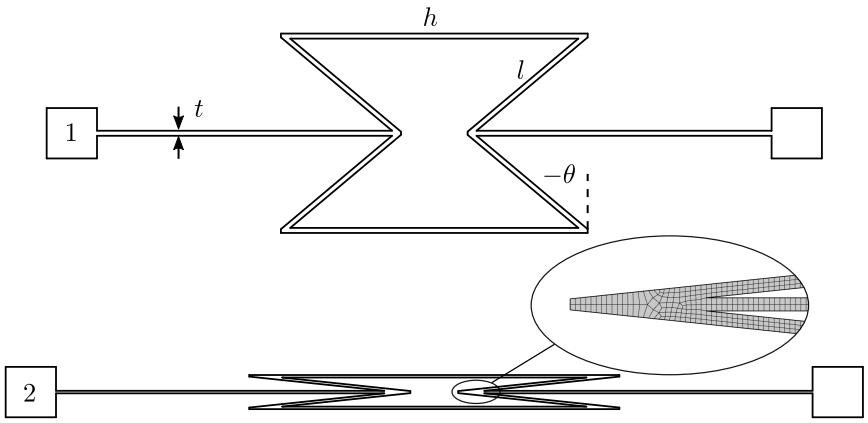

Figure E-2: Examples of geometries for $\theta = 50°$(1) and $\theta = 84°$(2).

In Figure E-2 two examples of the geometries used for the simulation. The quadrangular mesh indicated in the circle is for designs with $t = 0.5$ mm, with maximum element size 0.2 mm. The mesh used for designs with $t = 1$ mm has a maximum element size of $h = 0.4$ mm. The design parameters for all the designs is found in Table E-2.

θ [deg]	h [mm]	l [mm]	t [mm]
40	60	30	1
50	60	30	1
60	60	30	1
70	60	30	1
71	60	30	1
72	60	28	1
73	60	28	1
74	60	28	1
75	60	28	1
76	60	28	1
77	60	28	1
78	60	28	1
80	70	30	0.5
82	70	30	0.5
84	70	30	0.5

Table E-2: Design Parameters for Re-entrant structures used in the simulation. The minimal changes of h and l were necessary to make the geometry possible for larger angles of θ.

Appendix F

Processing Images

```
%%%%%%%%%%%%%%%%%%%%%%%%%%%%%%%%%%%%%%%%%%%%%%%%%%%%%%%%%%%%%%%%%%%%%%%%%%%%
% This Script is written by :   Bas Nederkoorn
% Date :                        14 - 09 - 2019
% Function : Analysis of images and determining displacement of auxetic
%%%%%%%%%%%%%%%%%%%%%%%%%%%%%%%%%%%%%%%%%%%%%%%%%%%%%%%%%%%%%%%%%%%%%%%%%%%%
function [centers_x,centers_y] = comparenodes(filename,diameter)
im_o = imread(filename);              % Import Image
radius = diameter/2;                  % Detect Green Marker Circles
im_o = im_o(500:2300,600:3000 , 2); % Cropping and Filter Image
im = im2bw(im_o,0.55);
bw = bwareaopen(im, 250);

[centers,radii] = imfindcircles(bw,[radius-10 radius+5],'ObjectPolarity',
    'bright','Sensitivity',0.86); % Retrieve Circles

if length(centers) > 140              % Check if all Markers are Seen
    im = im2bw(im_o,0.6);             % If not sensitivity is adjusted
    bw = bwareaopen(im, 250);
    [centers,radii] = imfindcircles(bw,[radius-10 radius+5],'
        ObjectPolarity','bright','Sensitivity',0.86);
end
if length(centers) < 140
    im = im2bw(im_o,0.5);
    bw = bwareaopen(im, 250);
    [centers,radii] = imfindcircles(bw,[radius-10 radius+5],'
        ObjectPolarity','bright','Sensitivity',0.86);
end

centers = sortrows(centers);          % Sorting Matrix to match location
sorted = zeros(10*14,2);              % in marker grid

for i = 1:14
    sorted(10*i-9:10*i,:) = sortrows(centers(10*i-9:10*i,:),2);
```

```
31 end
32 c_x = sorted(:,1);
33 c_y = sorted(:,2);
34 centers_x = reshape(c_x,[10,14]);    % Return x,y coordinates of
35 centers_y = reshape(c_y,[10,14]);    % every marker
36 end
```

Bibliography

[1] W. H. Organization, "Cardiovascular diseases." https://www.who.int/health-topics/cardiovascular-diseases/, 12. (Accessed on 12/08/2019).

[2] R. Ross, "The pathogenesis of atherosclerosis—an update," *New England journal of medicine*, vol. 314, no. 8, pp. 488–500, 1986.

[3] R. Erbel, M. Haude, H. W. Höpp, D. Franzen, H. J. Rupprecht, B. Heublein, K. Fischer, P. de Jaegere, P. Serruys, W. Rutsch, *et al.*, "Coronary-artery stenting compared with balloon angioplasty for restenosis after initial balloon angioplasty," *New England Journal of Medicine*, vol. 339, no. 23, pp. 1672–1678, 1998.

[4] W. Liang, Y. Huang, Y. Xu, R. K. Lee, and A. Yariv, "Highly sensitive fiber bragg grating refractive index sensors," *Applied physics letters*, vol. 86, no. 15, p. 151122, 2005.

[5] D. Hill and G. Cranch, "Gain in hydrostatic pressure sensitivity of coated fibre bragg grating," *Electronics letters*, vol. 35, no. 15, pp. 1268–1269, 1999.

[6] C. R. Dennison and P. M. Wild, "Enhanced sensitivity of an in-fibre bragg grating pressure sensor achieved through fibre diameter reduction," *Measurement science and technology*, vol. 19, no. 12, p. 125301, 2008.

[7] K. E. Evans and A. Alderson, "Auxetic materials: functional materials and structures from lateral thinking!," *Advanced materials*, vol. 12, no. 9, pp. 617–628, 2000.

[8] B. Nederkoorn, "Potential of metamaterials for improving pressure sensitivity of fiber bragg grating sensors - a literature review," *TU Delft Repository*, 2019.

[9] L. R. Meza, S. Das, and J. R. Greer, "Strong, lightweight, and recoverable three-dimensional ceramic nanolattices," *Science*, vol. 345, no. 6202, pp. 1322–1326, 2014.

[10] R. Gatt, L. Mizzi, J. I. Azzopardi, K. M. Azzopardi, D. Attard, A. Casha, J. Briffa, and J. N. Grima, "Hierarchical auxetic mechanical metamaterials," *Scientific reports*, vol. 5, p. 8395, 2015.

[11] K. K. Saxena, R. Das, and E. P. Calius, "Three decades of auxetics research- materials with negative poisson's ratio: a review," *Advanced Engineering Materials*, vol. 18, no. 11, pp. 1847–1870, 2016.

[12] W. Zhang, F. Li, Y. Liu, and L. Liu, "Ultrathin fbg pressure sensor with enhanced responsivity," *IEEE Photonics Technology Letters*, vol. 19, no. 19, pp. 1553–1555, 2007.

[13] R. C. Hibbeler and S. Fan, *Statics and mechanics of materials*, vol. 2. Prentice Hall Singapore, 2004.

[14] Y. Liu, Z. Guo, Y. Zhang, K. S. Chiang, and X. Dong, "Simultaneous pressure and temperature measurement with polymer-coated fibre bragg grating," *Electronics letters*, vol. 36, no. 6, pp. 564–566, 2000.

[15] A. Alomarah, D. Ruan, S. Masood, I. Sbarski, and B. Faisal, "An investigation of in-plane tensile properties of re-entrant chiral auxetic structure," *The International Journal of Advanced Manufacturing Technology*, vol. 96, no. 5-8, pp. 2013–2029, 2018.

[16] H. Li, Y. Ma, W. Wen, W. Wu, H. Lei, and D. Fang, "In plane mechanical properties of tetrachiral and antitetrachiral hybrid metastructures," *Journal of Applied Mechanics*, vol. 84, no. 8, p. 081006, 2017.

[17] I. Masters and K. Evans, "Models for the elastic deformation of honeycombs," *Composite structures*, vol. 35, no. 4, pp. 403–422, 1996.

[18] L. J. Gibson and M. F. Ashby, *Cellular solids: structure and properties*. Cambridge university press, 1999.

[19] D. Mousanezhad, B. Haghpanah, R. Ghosh, A. M. Hamouda, H. Nayeb-Hashemi, and A. Vaziri, "Elastic properties of chiral, anti-chiral, and hierarchical honeycombs: a simple energy-based approach," *Theoretical and Applied Mechanics Letters*, vol. 6, no. 2, pp. 81–96, 2016.

[20] A. Alderson, K. L. Alderson, D. Attard, K. E. Evans, R. Gatt, J. N. Grima, W. Miller, N. Ravirala, C. Smith, and K. Zied, "Elastic constants of 3-, 4-and 6-connected chiral and anti-chiral honeycombs subject to uniaxial in-plane loading," *Composites Science and Technology*, vol. 70, no. 7, pp. 1042–1048, 2010.

[21] J. N. Grima, R. Gatt, and P.-S. Farrugia, "On the properties of auxetic meta-tetrachiral structures," *physica status solidi (b)*, vol. 245, no. 3, pp. 511–520, 2008.

[22] K. Szykiedans, W. Credo, and D. Osiński, "Selected mechanical properties of petg 3-d prints," *Procedia Engineering*, vol. 177, pp. 455–461, 2017.